**Author Contributions:**

**Conceptualization:** R. Sulzbach, V. Klemann, H. Dobslaw, M. Thomas
**Data curation:** R. Sulzbach
**Formal analysis:** R. Sulzbach, H. Dümpelmann
**Investigation:** R. Sulzbach, V. Klemann, G. Knorr, H. Dobslaw, G. Lohmann
**Methodology:** R. Sulzbach, V. Klemann, H. Dobslaw
**Resources:** G. Knorr, G. Lohmann
**Software:** R. Sulzbach
**Supervision:** H. Dobslaw, M. Thomas
**Validation:** R. Sulzbach
**Visualization:** R. Sulzbach
**Writing – original draft:** R. Sulzbach, V. Klemann, G. Knorr

# Evolution of Global Ocean Tide Levels Since the Last Glacial Maximum

**R. Sulzbach**[1,2] , **V. Klemann**[1] , **G. Knorr**[3] , **H. Dobslaw**[1] , **H. Dümpelmann**[4], **G. Lohmann**[3] , and **M. Thomas**[1,2]

[1]German Research Centre for Geosciences GFZ, Potsdam, Germany, [2]Institute for Meteorology, Freie Universität Berlin, Berlin, Germany, [3]Alfred Wegener Institute Helmholtz Centre for Polar and Marine Research, Bremerhaven, Germany, [4]Technical University Aachen, Aachen, Germany

**Abstract** This study addresses the evolution of global tidal dynamics since the Last Glacial Maximum focusing on the extraction of tidal levels that are vital for the interpretation of geologic sea-level markers. For this purpose, we employ a truly-global barotropic ocean tide model which considers the non-local effect of Self-Attraction and Loading. A comparison to a global tide gauge data set for modern conditions yields agreement levels of 65%–70%. As the chosen model is data-unconstrained, and the considered dissipation mechanisms are well understood, it does not have to be re-tuned for altered paleoceanographic conditions. In agreement with prior studies, we find that changes in bathymetry during glaciation and deglaciation do exert critical control over the modeling results with minor impact by ocean stratification and sea ice friction. Simulations of 4 major partial tides are repeated in time steps of 0.5–1 ka and augmented by 4 additional partial tides estimated via linear admittance. These are then used to derive time series from which the tidal levels are determined and provided as a global data set conforming to the HOLSEA format. The modeling results indicate a strengthened tidal resonance by $M_2$, but also by $O_1$, under glacial conditions, in accordance with prior studies. Especially, a number of prominent changes in local resonance conditions are identified, that impact the tidal levels up to several meters difference. Among other regions, resonant features are predicted for the North Atlantic, the South China Sea, and the Arctic Ocean.

**Plain Language Summary** We discuss changes in ocean tides during the last 21,000 years. This time marks the Last Glacial Maximum when large parts of the Earth's surface were covered by ice and the sea level was more than 100 m lower than today. Such a low sea level means that many regions of the Earth became land and the ocean's depth changed markedly. The distribution of land and water dominates changes in the tidal levels like the spring or neap tide. With a tidal computer model recently developed by our group, we determine these tidal levels for different times steps from 21,000 years to today. Tidal levels are important for geologists who want to understand former sea level changes with samples found at ancient shorelines. As many of such samples were deposited at a specific tidal level, our modeled information will help them to relate their height to the mean sea-level. Of course, our model is not the only one that can estimate such changes, but we discuss the advantages of our recent development over previous tools available.

## 1. Introduction

Global mean sea level (GMSL) has been rising at a speed of 3.25 mm yr$^{-1}$ during the last three decades due to the increased rate of ice loss on the Greenland and Antarctic ice sheets, as well as thermal expansion of the ocean water and glacial mass loss (IPCC, 2022). This observation is fundamentally important for protecting low-elevation coastal areas, which are often densely populated, as the risk of flooding increases with the GMSL.

The relative sea level (RSL), which measures the observed sea level with respect to the coast, is more complex and depends on many factors, including changes in the GMSL, the geoid or vertical motion of the Earth's surface, for instance, caused by tectonics, local subsidence or by glacial isostatic adjustment (GIA). Changes of the RSL generate the main threat to coastal communities and ecosystems. In addition to RSL variations which typically act over centuries, or even millennia, changes in frequency and probability of extreme sea level events can have profound consequences for human or marine coastal life. Thus, the local sea level variability on short time scales is the second important factor to understand the development of coastal regions besides the RSL, as well as to quantify its impact. For example, storm surges have a much more significant impact during high astronomical

**Writing – review & editing:** R. Sulzbach, V. Klemann, G. Knorr, H. Dobslaw, H. Dümpelmann, G. Lohmann, M. Thomas

tides (storm tides). As they represent a huge part of the sea-surface variability at diurnal and semi-diurnal time-scales, the tidal levels are of high importance to understand the frequency of said extreme events and can change with the rising sea level (e.g., Idier et al., 2017; Schindelegger et al., 2018) or be subjected to long-period cycles of the Lunar tides (Peng et al., 2019).

## 1.1. Tidal Levels and Sea Level Reconstruction

A further aspect of tidal levels is their relevance for the interpretation of geological sea-level markers such as sea-level index points (SLIPs) or terrestrial limiting points as marine limiting points. Such geological or archeological samples do not represent the actual sea level height at the time of their deposition but the environmental conditions at which the specific specimen lived or was deposited or a specific structure was build up. For instance, typical shore facies can be separated into a sequence of different marsh environments like high tidal marsh (MHW [Mean High Water] to HAT [Highest Astronomical Tide]) or low tidal marsh (MLW [Mean Low Water] to MHW). Also, specific coastal sediments like coquina are found only below HAT (Garrett et al., 2020), or beach rock is usually formed between MLW and HAT (Stattegger et al., 2013 and Mauz et al., 2015 in Khan et al., 2017). Considering such a catalog of sea-level data types, tidal levels have to be considered to define a mean deviation of an indicator's height with respect to MSL and a corresponding uncertainty due to its specific indicative range (IR) (Hijma et al., 2015). Accordingly, the authors suggested providing estimates of relevant tidal levels together with further information when publishing sea level data in a unified way, and international initiatives usually follow these suggestions. In the so-called HOLSEA format for providing sea level data (Khan et al., 2019), a list of tidal levels is required for correcting the indicative meaning of respective data types: MLWS (Mean low water springs), MLWN (Mean low water neaps), MLLW (Mean lower low water), MLW, MTL (Mean tidal level), MHW, MHHW (Mean higher high water), MHWN (Mean high water neaps), MHWS (Mean high water springs), HAT. For details see the workbook instructions at https://www.holsea.org/archive-your-data.

Because it is a well-established fact that ocean tidal dynamics have significantly changed with time, the precise knowledge of the present-day tidal regime which relies on empirical observations (e.g., Cartwright, 1999; Schrama & Ray, 1994; Stammer et al., 2014) is of limited value for the interpretation of paleo sea level markers. Data-unconstrained ocean tide models can provide the required data (e.g., Schindelegger et al., 2018; Wang et al., 2021) which depend directly on (paleo)oceanographic conditions, changes of GMSL and RSL, tide generating forces and the configuration of the continental plates. The latter effects are most important on geological times of $10^6$ to $10^8$ a and must be considered for deep-time simulations (e.g., Davies et al., 2020; Green et al., 2017; Haigh et al., 2020), where the primary interest usually focuses on tidal dissipation and the evolution of the Earth-Moon-Sun system (e.g., Daher et al., 2021; Kagan & Sündermann, 1996). On shorter time-scales, the continental configuration can be considered as static, particularly on the temporal scale of the repeated glacial cycles during the Pleistocene. During this epoch, tidal dynamics are most considerably influenced by GMSL and RSL, which varied during the last million years globally by more than 100 m (Berends et al., 2021). SLIPs are abundant only after the Last Glacial Maximum (LGM), granting the sea level reconstruction an increased amount of accuracy and allowing comparisons to modeling results. Accordingly, many paleotidal studies target this epoch.

## 1.2. Paleotidal Studies Since the LGM

With the compilation of global paleo topographies (e.g., Peltier, 1994), that is, reconstructions of the RSL-history since the LGM (e.g., Tushingham & Peltier, 1992), global studies of the respective tidal regime could be conducted (e.g., Thomas & Sündermann, 1999). A common feature of most studies is the strengthening of the North Atlantic $M_2$ oscillation and, related to this, the semidiurnal tidal dissipation (e.g., Egbert et al., 2004), which can be explained by the lowered sea level, that drastically reduces the extent of shelf areas, which serve as an energy sink by turbulent bottom friction dissipation (e.g., Wilmes & Green, 2014) and enhances tidal resonance (e.g., Green, 2010). The energy dissipation diverts to the deep ocean, where barotropic tidal energy transitions into the internal tide, which ultimately induces diapycnal tidal mixing (e.g., Green et al., 2009; Wunsch, 2003), a process that is interlaced with the general ocean circulation and its associated meridional heat transfer from tropical to polar latitudes. When considering the increased tidal dissipation under glacial conditions in a climate model, significant impact, that is, strengthening, on the Atlantic Meridional Overturning Circulation (AMOC) is proposed by Schmittner et al. (2015) and Wilmes et al. (2019), who report special sensitivity to the poorly

constrained position of the Antarctic ice sheet grounding line (e.g., Hillenbrand et al., 2014) in line with Wilmes and Green (2014). Another repeatedly observed feature is the transition of the Arctic $M_2$ to a mega-tidal regime (Griffiths & Peltier, 2008, 2009), a possible trigger of Heinrich events (Arbic, MacAyeal, et al., 2004; Velay-Vitow et al., 2020).

While the mentioned global studies did not focus on extracting tidal levels, it is, in principle, possible to derive charts of tidal levels from paleotidal simulations, which can be applied for the interpretation of SLIPs. However, reversely, the reconstruction of the sea level history is typically constrained by SLIPs (and present-day geodetic data for GIA rates). GMSL changes during a glacial cycle are on a scale of tens to hundreds of meters (Clark et al., 2016), while changes in tidal levels are expected only on a few-meter scale. Therefore, the feedback-loop tidal level → sea level reconstruction → tidal level is feeble and global tidal reconstructions are reckoned as robust (Neill et al., 2010). While the sea level interpretation bias which arises from ignoring changes of the paleo-otidal regime is usually the order of a few percent of the sea level change, it is of more relevance in the region surrounding formerly glaciated areas, where land surface uplift and sea level rise can partially compensate each other (Hijma et al., 2015).

Despite the outlined relevance, paleotidal changes are only discussed in a limited number of paleo sea level studies on SLIP-driven sea level reconstructions since the LGM which contribute to the HOLSEA global sea level data set of Khan et al. (2017). Horton et al. (2013) recommended combining a regional with a global tidal model when reconstructing paleo-tides and interpolating in time from sufficiently high resolved time-slices, for example, all 1-ka intervals as was done in Ward et al. (2016). To apply such a model combination was motivated by Uehara et al. (2006) who had found a significant increase of MHWS before 10 ka BP (before present) by 25%–50%, whereas the modification after 8 ka BP was reduced. Nevertheless, the modeling effort is huge, and the numerical cost of regional densification likely exceeds that of the global model (Griffiths & Hill, 2015). Such a model setup was applied mainly for the Northwest European shelf seas (Uehara et al., 2006; Ward et al., 2016), and North Atlantic west coast from the Artic to the Caribbean (Hill et al., 2011). The model of Hill et al. was applied by Horton et al. (2013) to the US Atlantic Coast, by Khan et al. (2017) to the Caribbean and by Vacchi et al. (2018) to those sites of the Canadian Atlantic. The model of Ward et al. (2016) was applied, for instance, by Barnett et al. (2020) for the evolution of the Scilly Island and by Vasskog et al. (2019) for the Norwegian coast.

To overcome numerical modeling of regional tidal solutions, different approximations are considered to estimate regional paleotidal changes. For instance, Cooper et al. (2018) suggested using modern tidal levels in the region of South Africa, where he applied tides of nearby lagoons of similar shape to those reconstructed from paleo shorelines. Hijma and Cohen (2019) considered the evolution of the flood basin in the Rhine-Meuse delta during the Holocene sea-level rise by increasing the tidal amplitude as a function of the estimated evolution of the flooded basin. A similar approach was discussed in Uehara and Saito (2019) for Tokyo Bay, where in addition a numerical tidal model was applied. Another solution is to increase the uncertainties of the considered tidal levels and accordingly the indicative range (e.g., Briggs & Tarasov, 2013; Hijma et al., 2015).

### 1.3. Objective and Outline of This Study

In this study, we present a global reconstruction of tidal levels since the LGM (21 ka BP) with a temporal resolution of 0.5–1 ka, that allows for tracking the temporal evolution of IRs for each arbitrary, coastal location on the globe. To achieve this, we employ a modern, data-unconstrained ocean tide model, which is validated for present-day conditions by geodetic data sets (Sulzbach et al., 2021). The employed model combines several key characteristics, which have to our knowledge not yet been considered in combination for paleo studies, (C1) a non-local implementation of the Self-Attraction and Loading effect (SAL), (C2) a "truly-global" domain (i.e., no open boundaries), (C3) the simulation of four major partial tides for each epoch, and (C4) a paleo bathymetry derived from the RTopo-2 bathymetry (Schaffer et al., 2016) and the ICE-7G reconstruction. In addition, we based the extraction of tidal levels on a broad data basis, by extending the tidal ensemble to eight major tides by linear admittance theory (C5). The so-created paleotidal data is used to synthesize time series and rigorously extract a set of 9 tidal levels for interpreting SLIPs. As a result, an easy-to-use, global data set of dense temporal resolution is provided. The spatial resolution of $\frac{1}{6}^{\circ}$ is fit to precisely capture the evolution of large-scale tidal resonances that govern the apparent tidal regime, while increased uncertainties remain in extended shelf seas. To further facilitate the derivation of regional paleotidal models, we also provide tidal transports and elevations

for selected partial tides which are necessary to derive realistic boundary conditions for those models. This comprehensive analysis of paleotidal levels is complemented by assessing the global tidal dissipation, which can provide valuable constraints for paleoclimate modeling and corroborates our findings by allowing comparisons to other, formerly conducted, paleotidal studies.

After this introduction, the paper is structured as follows: In Section 2, we introduce the numerical code, discuss the employed methods to extract the selected observables (tidal levels and dissipation), and validate the model. Afterward, we recapitulate the construction of paleo oceanographic conditions in Section 3 that are the basis for the simulations presented thereupon in Section 4. Here, observed tidal resonances are discussed, which are characteristic of individual partial tides and often affect global dissipation. Separately, results for global tidal levels are presented. We close this study with Section 5, presenting a summary and an outlook toward possible future research directions. Additionally, we draw conclusions for employing the provided data set for the interpretation of SLIPs, which is illustrated as an example for the Hudson Bay region.

## 2. Barotropic Tidal Modeling

To obtain estimates of tidal dynamics and tidal levels during the last 21 ka BP, we employ a non-assimilative ocean tidal model, that we optimize for the accurate prediction of present-day tides on a global scale. In the following subsections, this model is introduced and discussed with respect to its performance at present-day conditions, the extraction of tidal levels, and tidal dissipation.

### 2.1. Numerical Model

We employ the barotropic ocean tidal model TiME as described by Sulzbach et al. (2021) that is unconstrained by empirical data (e.g., tide gauge, satellite altimetry, satellite gravimetry). The model is run in a global $\frac{1}{6}^\circ$-grid with numerical poles located in East Asia and South America (*chi*-configuration). The simulation is set up to dissipate energy dominantly by quadratic bottom friction and topographic wave drag (setting W0 of Sulzbach et al. (2021) with eddy viscosity coefficient $A_h = 2 \times 10^3 \, \mathrm{m^2 \, s^{-1}}$) dissipation mechanisms, which are theoretically well founded and understood. Thus, this setup also possesses a high degree of reliability in altered (paleo-)oceanographic conditions (Arbic et al., 2008; Egbert et al., 2004). Within, the model includes wave drag dissipation by a parameterization introduced by Nycander (2005) that is directly inferred from information about ocean stratification and bathymetry. The bathymetry $H$ is derived from the RTopo-2 data set (Schaffer et al., 2016). The effect of Self-Attraction and Loading (SAL) that exerts a strong influence on tidal dynamics (Ray, 1998) is included by spherical harmonic decomposition and load Love numbers (e.g., Schindelegger et al., 2018). In contrast to the local approximation of SAL, $\zeta_{SAL} = \epsilon\zeta$ (Accad & Pekeris, 1978), that relates SAL to local sea surface elevation $\zeta$ by a constant $\epsilon$, here the non-local (i.e., global) gravitational interaction of water masses mediated by SAL is considered. The unapproximated, in-line inclusion of SAL in TiME is in contrast to most previous studies that model paleotides over recent glacial-interglacial cycles (cf. Section 1.2), that with exception of Hill et al. (2011), employ local approximations, iterative approaches, or completely neglect the effect.

Changes in sea ice and shelf ice cover are prominent features of glacial-interglacial climate variations (e.g., CLIMAP-Project-Members, 1981; Jakobsson et al., 2014; Sejrup et al., 2000; Stein et al., 2017; Tarasov et al., 2012). Therefore, in addition to the TiME model characteristics documented in Sulzbach et al. (2021), we consider the long-range interaction of the barotropic ocean flow with floating ice, possibly exhibiting a drift velocity $\mathbf{v}_{\mathrm{ice}}$, by introducing the barotropic acceleration (cf. Figure 1a)

$$\mathbf{a} = \frac{r_{ice} \, f_{\mathrm{ice}}}{H} \, |\mathbf{v}_{\mathrm{rel}}| \, (\mathbf{v}_{\mathrm{ice}} - \mathbf{v}) \tag{1}$$

into the numerical model (e.g., Bij de Vaatie et al., 2021; Cancet et al., 2016; Kagan & Sofina, 2009; Müller et al., 2014). This acceleration is structurally identical to quadratic bottom friction, where the bottom friction coefficient $r = r_{ice}$ is retained (doubled bottom friction), but the relative velocity between ice and ocean flow, $\mathbf{v}_{\mathrm{rel}} = \mathbf{v}_{\mathrm{ice}} - \mathbf{v}$, controls the dynamics and is constrained by the fractional ice cover $0 < f_{\mathrm{ice}}(\boldsymbol{x}) < 1$, where $\boldsymbol{x} = (\lambda, \phi)$ denotes the longitude-latitude pair. It is important to note that this parameterization induces two distinct effects. First, a dissipative, dampening effect proportional to $-\mathbf{v}$, similar to bottom friction, and second an acceleration proportional to $\mathbf{v}_{ice}$, denoted $\boldsymbol{a}_{ice}$, that will induce a residual, non-periodic circulation. The later considered realizations of $\mathbf{v}_{ice}$ and $f_{ice}$ are shown in Figures 1b and 1c.
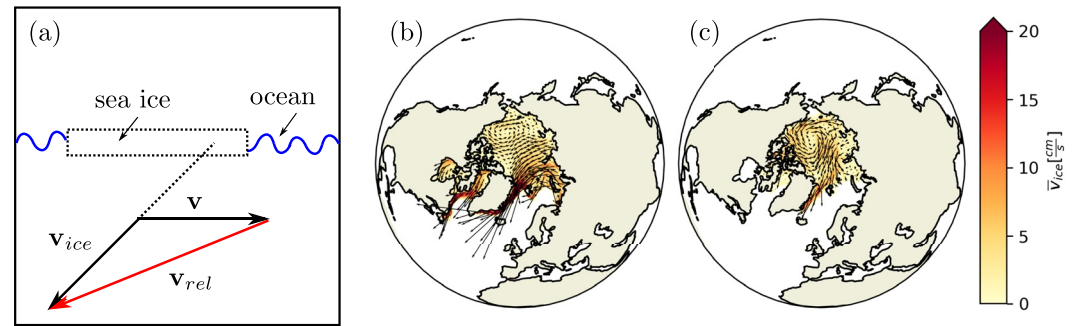
**Figure 1.** Climatological sea ice coverage and ice drift velocity $\mathbf{v}_{ice}$ (1995–2019) for winter (FMA, b) and summer (ASO, c) conditions, where arrows indicate drift directions. Ice friction is proportional to the relative velocity $\mathbf{v}_{rel}$ as indicated by (a), containing a purely dissipative part proportional to $-\mathbf{v}$ and a second part proportional to $\mathbf{v}_{ice}$ that excites a barotropic background circulation.

Altogether, TiME integrates the nonlinear shallow-water equations to simulate barotropic ocean dynamics, which are forced with the tide raising-potential (TRP) (cf. Sulzbach et al., 2021; Sulzbach, Wziontek, et al., 2022). Within this study, we only consider the individual excitation of partial tides (frequency $\omega$) as listed in the tide-generating potential (TGP) HW95 (Hartmann & Wenzel, 1994, 1995), that is, setting the potential proportional to $\overline{P}_{lm}(\sin\theta)\cos(\omega t + m\lambda)$, where $\overline{P}_{lm}$ are the normalized associated Legendre polynomials (partial tide forcing mode). Disregarding minor, nonlinear tides, we extract the harmonic constituents for a partial tide, with label $i$, the amplitude $A^i_{mod}(\mathbf{x})$ and Greenwich phase lag $\psi^i_{mod}(\mathbf{x})$, for the sea surface elevation after an initialization time of at least 1 month, denoted

$$\zeta^i_{mod}(t) = A^i_{mod}\cos(\omega t - \psi^i_{mod}) \ . \tag{2}$$

Comprising the results of this section, TiME is employed as a transformation operator that translates a certain partial tide-raising potential into the respective ocean tidal response described by $A^i_{mod}$ and $\psi^i_{mod}$, considering the relevant oceanographic conditions.

With respect to other ocean tide models adapted to paleo conditions, the presented TiME configuration primarily distinguishes itself by the combination of two properties that were not considered together by other studies, which are the implementation of the non-local effect of SAL (C1), and a truly-global grid (C2), that allows the unbiased investigation of Arctic tides (cf. Section 1.3). Additional novel features are the implementation of the Nycander wave drag scheme with estimated paleo stratification data and the ice friction effect, which did not considerably impact the study, as we will show. The model resolution of $\frac{1}{6}^\circ$ is among the higher resolving models, even though several earlier studies employ resolutions of $\frac{1}{8}^\circ$ (e.g., Wilmes et al., 2019) and even higher (e.g., Velay-Vitow et al., 2020).

## 2.2. Model Setup and Validation

To validate the model results for present-day tidal conditions, empirical data is employed. In order to further quantify the impact of the newly introduced ice friction parameterization, we consider a set of 3 simulation experiments: no sea ice (*mod*), non-drifting sea ice (*mod-ice*), drifting sea ice (*mod-ice-v*). Validation of tidal solutions is pursued by employing bottom pressure records (BPR) compiled by Ray (2013) and the data-constrained tidal model FES14 (Lyard et al., 2021) for the main lunar $M_2$-tide. We calculate the root-mean-square error (RMSE) between TiME and the data sets, where the comparison to FES14 is restricted to a non-polar ($|\varphi| < 66°$) open ocean (H > 1,000 m) domain. For experiment *mod*, an RMSE of 6.78 cm (FES14) and 6.05 cm (BPR) is obtained. Compared to the results obtained on a $\frac{1}{12}^\circ$-grid by Sulzbach et al. (2021) the employment of experiment *mod* leads to an RMSE-increase of 2.66 and 1.95 cm, respectively. Similar results are obtained with experiments in *mod-ice* and *mod-ice-v* hinting at a minor improvement by an RMSE reduction on the mm-level. An inter-comparison of the three experiments reveals that the most significant deviations due to sea ice friction arise in the direct vicinity of shallow, ice-covered regions and a smaller impact in the northern mid-latitudes. For a more detailed discussion of the ice-effect, we refer to the Supporting Information of this article.

Evaluating the global dissipation of the $M_2$ partial tide, we find 2.49 TW (1 TW = 1000 GW = $10^{12}$ J/s) for *mod* with only minor changes for the other experiments. Here, the dissipation by ice friction is found to be considerably affected by winter (134 GW) and summer (46 GW) conditions in the Northern hemisphere (cf. Müller et al., 2014). Figures 1b and 1c show the most prominent differences in seasonal ice coverage which are found in the Hudson Bay and Hudson Straight, that is, shallow marginal seas that are known to possess relatively large $M_2$ flow amplitudes. As the sea ice friction, Equation 1, is proportional to $H^{-1}$ and $|\mathbf{v}_{rel}|$, this points to an important prerequisite for ice friction to impact tidal dynamics: The ice coverage must take place in shallow seas with large tidal flow velocities. On the one hand, the impact of sea ice was relatively small compared to the mean tidal signal for the modern $M_2$ tide. On the other hand, the extent of shallow shelf seas is known to reduce toward the LGM (Wilmes & Green, 2014). Hence, we ignore the effect of sea ice in the presented simulations. However, we will present additional simulations considering exaggeratedly expanded sea ice (pole-wards of $|\varphi| = 45°$) to estimate the maximum effect of sea ice.

As TiME is barotropic and has been optimized for open ocean dynamics, the validation in this section primarily targeted those areas with less precise representation of shelf and coastal regions. However, because SLIPs are inherently located in coastal vicinity, we discuss the accuracy of TiME concerning reconstructed coastal tidal levels based on tide gauge data in the next section.

### 2.3. Reference Levels for Tidal Heights

Tidal levels such as MLLW to HAT introduced in Section 1 describe the periodic sea surface variability at a specific location. In principle, they are composed of several harmonic constituents with frequencies related to celestial mechanics (e.g., Bretagnon, 1982; Doodson, 1921). This temporal harmonic behavior can be described by

$$\zeta_{\text{mod}}(t) = \sum_{i}^{N} A_{\text{mod}}^{i} \cos\left(\phi_i(t) - \psi_{mod}^{i}\right), \tag{3}$$

where $\phi_i(t) = \sum_{j=1}^{6} k_j^i \, \lambda_j(t) + k_7^i \frac{\pi}{2}$, is a combination of astronomical arguments $\lambda_j$ multiplied with integers (i.e., related to Doodson numbers) and $k_7^i \frac{\pi}{2}$ is the Doodson-Warburg phase shift related to the definition of the TGP (Petit & Luzum, 2010). While an elaborate tidal analysis of the TGP (here: Hartmann & Wenzel, 1994; Hartmann & Wenzel, 1995) and sea surface dynamics (e.g., Lyard et al., 2021; Piccioni et al., 2019) is typically composed of a large number of constituents, the most significant part of the variability can be captured by considering $N = 8$ major tidal constituents. These partial tides, comprising four diurnal ($K_1$, $O_1$, $P_1$, and $Q_1$) and four semidiurnal ($M_2$, $S_2$, $N_2$, and $K_2$) constituents, are employed to predict global ocean tidal dynamics for a given epoch. To reduce the computational effort, only two partial tides per tidal band ($M_2$, $K_2$, $K_1$, and $O_1$) are simulated. The residual four tidal solutions are estimated by assuming the ocean admittance function (complex tidal amplitude normalized with the astronomical excitation amplitude) to be a linear function of the excitation frequency $\omega$. This *linear admittance* approach builds upon the assumption that barotropic ocean tidal dynamics are only weakly nonlinear in $\zeta$ and $\omega$ (for small $\delta\omega$); a fact that is well-confirmed by observational data for present-day tides (e.g., Hart-Davis, Dettmering, et al., 2021; Munk & Cartwright, 1966; Rieser et al., 2012).

To discuss tidal amplitudes, we follow three approaches. The considered major partial tides are predominantly varied only by integral multiples of the mean lunar time $\tau$ (diurnal), the mean lunar longitude $s$ (monthly), and the mean solar longitude $h$ (annually). Solely $Q_1$ and $N_2$ are impacted by variations of longer period (mean longitude of the lunar perigee, 8.85 yr). As they are below the smaller amplitude components of the considered tides, we decided to neglect this long-period variation of $Q_1$ and $N_2$ and consider Equation 3 for 1,000 lunar days (approx. 3 yr), evaluating 65 time steps per lunar day. The astronomical arguments within $\phi_i(t)$ are evaluated employing the development of J. L. Simon et al. (1994). The resulting time series (cf. Figure 2) is then further processed to derive tidal levels for MLLW, MLW, MHW, MHHW, and HAT (approach A). Therein, the tidal levels or datums are defined as statistical measures of the high-tide or low-tide variability. MTL was found to be on the order of only a few cm and thus can be assumed to be zero within this approach.

SLIPs are typically found in coastal proximity. Therefore, we validate the accuracy of the derived tidal levels with respect to a set of coastal tide gauges as a proxy for the accuracy of paleotidal levels. For this purpose, we utilize the tide gauge data set TICON (Piccioni et al., 2019) consisting of 1145 tide gauge stations with 40 tidal constituents (amplitude: $A_{\text{tg}}^{i}$; phase: $\psi_{\text{tg}}^{i}$) each and derive tidal levels by two means: First, by employing the identical
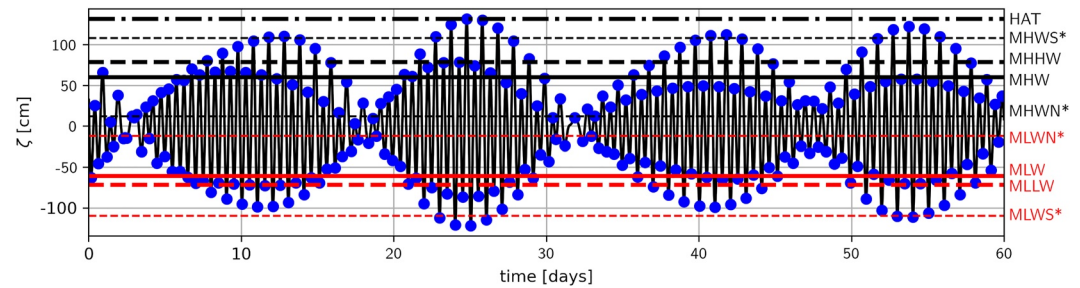
**Figure 2.** Example time series (60 days) and derived tidal levels synthesized of eight main partial tides (black curve) at Gulf Saint Vincent, Australia (35°S, 138.3°E) for present-day conditions. High and low tides (blue points) are used to derive the tidal levels (horizontal lines). As the tidal constituents for $S_2$ and $M_2$ have nearly equivalent amplitude, the time series shows a pronounced spring/neap-asymmetry. Spring/neap tide-related parameters derived with the help of $p_{\pm}$ (cf. Equation A1) appear with an asterisk.

procedure as for TiME (eight major tides, 1,000 lunar days: approach B) and second, by considering 29 partial tides of TICON for 7,000 lunar days covering multiple cycles of the lunar perigee (29 partial tides, approach C). Only nonlinear and seasonally-modulated tides that are not included in HW95 ($M_8$, $S_4$, $S_3$, MKS, $MS_4$, $R_2$, $MA_2$, and $MB_2$) and minor, long-period tides ($M_{sf}$, $M_{sq}$, $M_{tm}$) are ignored.

To quantify the mean agreement between two approaches, $x$ and $y$, we calculate the RMSE and normalize it to the mean quadratic amplitude obtained from the second data set, $y$, thus expressing the mean captured signal fraction $c(x, y) = 1 - \text{RMSE}(x, y)/\text{RMSE}(0, y)$, which takes values between 100% (perfect agreement) and $-\infty$. We find a high mean agreement for approaches B and C between 92.3% (HAT) and 97.2% (MLLW), indicating that eight major tides and simulation for 1,000 lunar days will be sufficient to predict tidal levels to a high level of accuracy. In the next step, tidal levels are calculated on the rotated TiME grid (*chi*) and are interpolated (nearest-neighbor interpolation) to standard coordinates employing the coordinate transformation as depicted in Sulzbach et al. (2021), in this way representing approach A. This approach was preferred, because interpolating on the rotated grid is the most precise possibility for predicting near-coastal tidal levels. We find a mean captured signal fraction of 70.6% (HAT) and 71.7% (MLLW) between approaches A and B. Recalling the results for approaches B and C, we conclude that the mean agreement between predicted and measured tidal levels is at a level of 65%–70%, when employing approach A.

The results for approaches A and C are presented in Figure 3. The plots generally indicate a close match between TiME and TICON, with larger relative deviations in micro-tidal marginal seas (e.g., Baltic, Mediterranean) and moderately reduced agreement in extended shelf seas (e.g., European shelf) in comparison to the deep ocean where the agreement is highest. While it was to be expected that a global tidal model with comparably low
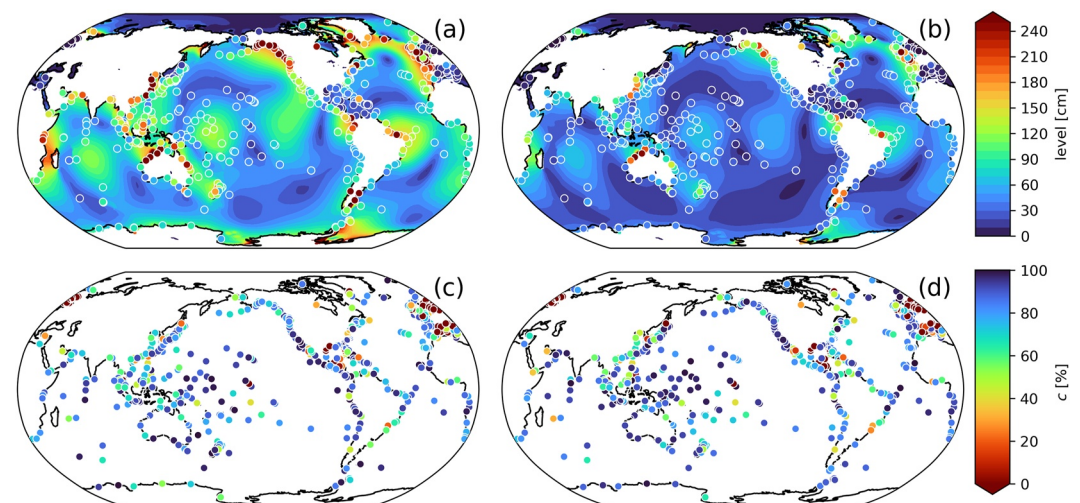


**Figure 3.** Tidal levels as derived from TiME (approach A, global field) and TICON (approach C, circles) in cm, exemplary for HAT (a) and MHW (b), and respective agreement $c$ in % at tide gauge stations (c, d).

resolution in coastal areas would exhibit increased deviations with coastal tide gauges, the apparent level of 70% is still satisfactorily high. In addition, we will focus on the temporal evolution of model differences between epochs that are likely to partially absorb systematic model deviations.

To enlarge the procured set of tidal levels, we further estimate the parameters MLWN, MLWS, MHWN, and MHWS. To achieve this, MLW and MHW are multiplied with a factor $p_\pm$ based on the tidal amplitudes of the two largest tides per tidal band ($M_2$ and $S_2$ vs. $K_1$ and $O_1$) that are the main drivers for spring/neap-cycles (cf. Appendix A). Please note that those parameters exhibit an increased amount of uncertainty due to the qualitative nature of this approach but integrate reasonably into the set of directly derived parameters. As an example, Figure 2 shows a synthetic 60 day time series from Gulf Saint Vincent. Due to comparably strong $S_2$ and $M_2$ constituents, this location is known to exhibit a pronounced spring/neap tide cycle, locally known as *dodge tide*, which is reasonably well predicted by employing $p_\pm$.

The employed extraction scheme for tidal levels features two key elements, which were not considered in prior paleotidal studies (cf. Section 1.3). First, the continuous simulation of 4 partial tides per epoch (C3), and second the linear admittance constrained extension to 8 partial tides with the proper extraction of tidal levels for the interpretation of SLIPs (C5).

### 2.4. Tidal Resonances and Dissipation

Tides mediate energy transfer in the Earth–Moon–Sun system by frictional processes controlling, for example, the evolution of the lunar orbit (Daher et al., 2021; Green et al., 2017; Kagan & Sündermann, 1996; Mignard, 1979; Ray et al., 2001). Within, the predominant part of present-day ocean tidal dissipation is carried out through turbulent bottom friction on the continental shelves and excitation of internal waves in the deep ocean (Egbert & Ray, 2000; Nycander, 2005). For example, the main lunar ocean tide $M_2$ dissipates 2.45 TW, of which about 1 TW can be attributed to the generation of internal waves in the deep ocean (Egbert & Ray, 2001). As internal waves ultimately dissipate their energy by breaking into turbulent mixing (St. Laurent et al., 2002), they can influence baroclinic processes as the MOC, thus ultimately linking the tidal regime of a particular epoch to its climate (Müller et al., 2010; Schmittner et al., 2015; Wilmes et al., 2019). Therefore, predicting and monitoring tidal dissipation can provide boundary conditions for paleoclimate reconstructions and the evolution of the lunar orbit. Furthermore, it can serve as an additional benchmark for validating present-day tidal models with observations of tidal dissipation. Thus, tidal dissipation was selected as an additional model output in addition to the tidal levels discussed in the previous section.

Assuming linear admittance, the global dissipation of tides of identical degree (here $l = 2$) and order (here $m = 1$, 2) follows the equation

$$\overline{D}_i = (\alpha_2(\omega_i) A_i)^2 (c_{2m}^0 + c_{2m}^1 \omega_i), \qquad (4)$$

where $A_i$ is the amplitude of the TGP, $\alpha_2$ is a combination of body tide Love numbers and $c_{2m}^i$ are constants stemming from global integrals of $\mathbf{v}_i$ and $\nabla Y_{2m}$ (cf. Appendix B). As two partial tides per tidal band $m$ are simulated, the $c_{2m}^i$ can be extracted, thus allowing the exploitation of Equation 4 to estimate dissipation by additional partial tides.

Tidal sea surface height variations estimated by linear admittance are proportional to $A_i$. In contrast, Equation 4 is proportional to $A_i^2$. Thus tidal dissipation concentrates on the highest amplitude tides diminishing quickly for minor tides. Attention has to be paid when employing this approach, as dissipation estimates can change the sign for far-extrapolated tides. This nonphysical behavior should be discarded as an artifact of the linear admittance approach, but it did not occur in our simulations.

Applying this approach for present-day tidal dynamics, we obtain a total dissipation by the considered major tides of 3682 GW (partitioning as $M_2$: 2494 GW, $S_2$: 481 GW, $K_1$: 334 GW, $O_1$: 199 GW, $N_2$: 97 GW, $K_2$: 35 GW, $P_1$: 34 GW and $Q_1$: 8 GW). These results match the reference values for Earth–Moon–Sun dissipation (3.7 TW) and pure $M_2$-dissipation of 2.45 TW (Egbert & Ray, 2001). Clearly, the dissipation is dominated by $M_2$ to $O_1$ with only minor contributions from the other four frequencies.

Employing the presented linear admittance approach it is possible to estimate the temporal evolution of the global tidal dissipation by all 8 major tides, not only $K_1$ and $M_2$, that dominate the dissipation spectrum. By this, the uncertainty of global deep ocean dissipation is reduced.

## 3. Paleotidal Conditions

In this section, we discuss changes of the paleoceanographic conditions which impact the tidal regime mapped by the ocean tide model introduced in the last section. While changes in of the Coriolis parameter, the tide-raising potential and the surface gravity are negligibly small in the time span of interest, we focus on changes in non-astronomical factors, that are known to be relevant on the discussed time scale from prior studies (e.g., Wilmes & Green, 2014; Haigh et al., 2020; Daher et al., 2021).

Changes of the paleoclimate are expected to impact the quantity and distribution of sea and shelf ice. As floating ice masses interact with the mean tidal flow via frictional forces these changes can in principle effect the paleo-tidal dynamics. Due to the reasons discussed in Section 2.2, we ignore the effect of sea ice friction and restrain ourselves to evaluate a number of estimates by considering extreme ice coverage for certain time slices (7.5, 10, 12.5, 15, 17.5 ka BP).

Second, the changed climatic conditions impact the stratification of the ocean and therefore the coupling between the here studied barotropic ocean tides and their baroclinic counterparts (internal tides) that can be parameterized as topographic wave drag (e.g., Bell, 1975; Llewellyn Smith & Young, 2003; Nycander, 2005). Estimates for ocean stratification were obtained from three different climate simulations (Sun et al., 2022; Zhang et al., 2013) for pre-industrial, LGM and deglacial conditions using the fully coupled Earth system model (COSMOS) (Jungclaus et al., 2010). The corresponding climate states for pre-industrial and the LGM (21 ka BP) are experiments PI and LGMW from Zhang et al. (2013). The deglacial state is representative of conditions at 16 ka BP at a time of substantial ice sheet disintegration and associated meltwater flux to the North Atlantic, which has been simulated as experiment 16K_0.21 in Sun et al. (2022). For technical details of the model components, model configuration and experimental set-up we would like to refer to these studies and references therein. Employing these data sets, we constructed topographic wave drag tensors (Nycander, 2005) for diurnal and semi-diurnal tidal species for four different epochs: First, we assume modern conditions as described in Sulzbach et al. (2021) utilized for times slices 0 to 0.5 ka BP (regime *I*). Further, preindustrial conditions for time slices 0.5 to 7.5 ka BP (regime *II*), Heinrich-stadial conditions before the Bølling/Allarød (B/A) for time slices 7.5 ka BP to 18.5 ka BP (regime *III*) and LGM-conditions from 18.5 to 21 ka BP (regime *IV*) were employed. Already anticipating the results of the following section, we found the impact of the changed wave drag dissipation to be of minor importance. Admittedly, the impact of the altered ocean stratification on the vertical current profile and, connected to this, the tidal ocean bottom friction was not considered in this study, while this effect is known to impact the seasonal variations of $M_2$ (Howarth, 1998; Müller et al., 2014). The quantification of this effect would be an intriguing application of a global, baroclinic paleocean tidal model and is thus out of the scope of this study.

The most considerable influence on ocean tides is known to originate from changes in the bathymetric conditions triggered by glaciation and deglaciation processes (e.g., Griffiths & Peltier, 2008; Thomas & Sündermann, 1999; Velay-Vitow et al., 2020). These bathymetric changes, implicitly including progressing and receding shorelines, directly impact the barotropic resonance conditions that can be elegantly described by a set of ocean normal modes (e.g., Müller, 2007). Reconstructing the sea level history is complicated, as it is not sufficient to know the amount of water bound in ice sheets, that is, the GMSL. Additionally, the local sea level is impacted by changes in the Earth' shape, the Geoid, that is again controlled by mass redistribution in the ocean, glaciers and the solid Earth. These changes depend on quantities like the mantle viscosity, the insolation and the resulting global ice history that exhibit large uncertainties but control the effect of glacial isostatic adjustment (GIA) (e.g., Abe-Ouchi et al., 2013).

Modern geodetic techniques such as GNSS or satellite gravimetry set precise, large-scale constraints for uplift-rates due to GIA and therefore effectively reduce the uncertainty of the respective reconstruction.

In this study, we rely on the reconstruction ICE-7G_NA that considers a comprehensive amount of said constraining data on the North American continent (Roy & Peltier, 2015, and references therein). Even though no constraining data was used in this area, Roy and Peltier (2018) showed that the obtained sea level reconstruction agrees well with SLIPs in the Mediterranean and also certain far-field areas. To obtain high-resolution bathymetric maps we employ the data set RTopo-2 (Schaffer et al., 2016) to derive a bathymetric map for modern conditions as described in Sulzbach et al. (2021), that is, containing sub ice shelf cavities as free water column. Paleobathymetries are obtained by modifying these high resolution data sets by the topographic and bathymetric differences from ICE-7G_NA. As a result, a set of high-resolution bathymetries is obtained for individual time slices (cf.
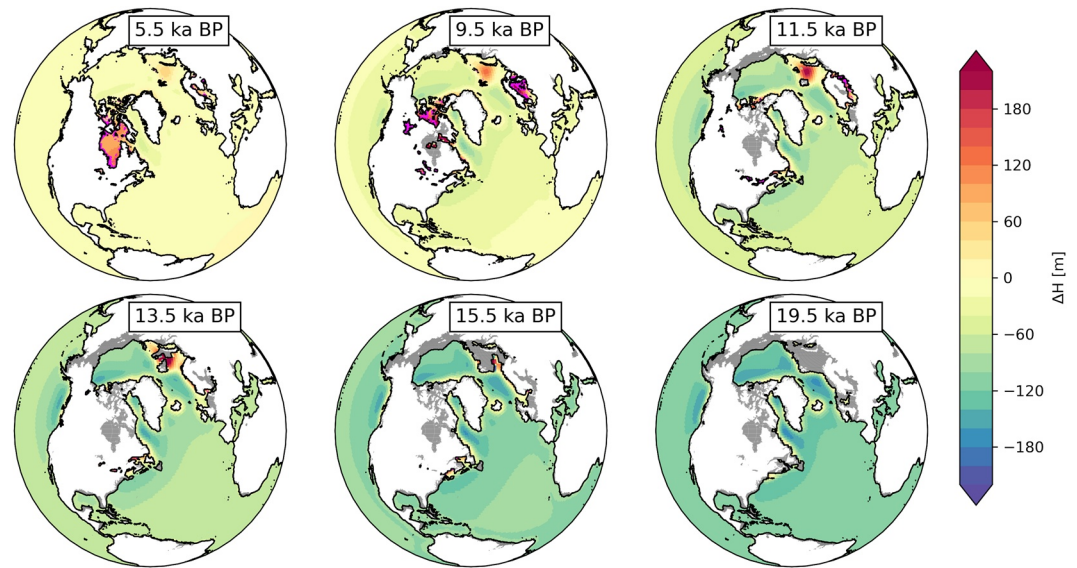
**Figure 4.** Relative depth change with respect to the present-day bathymetric map (0 ka BP) in meter. Coastlines are drawn as for the respective epoch, with increased land area in gray and flooded grid cells in magenta (Hudson Bay, Baltic ocean). As the topography considers ice sheets, areas of northern Canada, Barents Sea and Baltic appear gray due to ice cover.

Figure 4). Due to changes in the geoid, the sea level might rise locally. Therefore, it is important to also allow apparent sea-level rise, when calculating paleobathymetries, which is considered here. This phenomenon is most notable in the Baltic Sea and Hudson Bay. While this study is not focused on estimating the impact of different paleo reconstructions as, for example, Wilmes and Green (2014) and Wilmes et al. (2019), the combination of ICE7G and RTopo-2 has to our knowledge not been considered, yet. We will focus on comparing the obtained dissipation rates to results obtained by others.

To conclude this discussion it is important to mention that uncertainties in the Antarctic grounding line are not considered within this study. Nonetheless, we acknowledge that this effect could considerably impact the obtained tidal levels, also on the northern hemisphere, and therefore represents a source of uncertainty withing this study (Wilmes & Green, 2014; Wilmes et al., 2019).

## 4. Paleo Ocean Tidal Dynamics

Now, we discuss the results of the paleotide simulations. First, we focus on changes of the partial tide oscillation systems and the accompanying shifts in tidal dissipation. Afterward, consequences for tidal levels are discussed, focusing on a number of exemplary regions that exhibit the most notable changes in tidal levels. Basin-masks are obtained from the World Ocean Atlas 2009 (Levitus, 2009) with the mask for Hudson Bay adjusted for the increased sea level.

### 4.1. Tidal Resonances and Dissipation

The following discussion relates to the tidal dissipation displayed in Figure 5. Please also consider changes in tidal amplitudes in Figures S2 to S9 in Supporting Information S1. Going backward in time, we first note that changes in tidal dissipation are relatively small until approximately 9 ka BP, where the shelf area fraction begins to decrease, which is in line with the findings of (Wilmes & Green, 2014). A notable variation in this period is the slightly augmented $M_2$-resonance in the Hudson Straight and Hudson Bay that peaks at 4.5 ka BP and later at 8 ka BP. The reason for this is the locally-increased sea level with respect to the present-day sea level (e.g., K. M. Simon et al., 2014), which improves the coupling between shelf sea and open ocean. Thereby it induces a slight decrease in dissipation and a drop in the North Atlantic $M_2$-amplitude (Uehara et al., 2006), and can be understood in terms of a coupled oscillator model (Arbic & Garrett, 2010). The feedback of the improved shelf resonance on the open ocean is significant as the dominant semidiurnal eigenmode of this region is known to be near resonant to the $M_2$-frequency (Arbic et al., 2007).
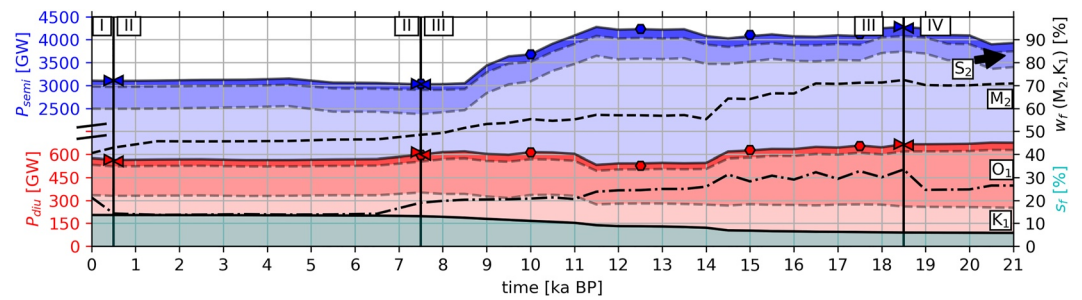
**Figure 5.** Cumulative tidal dissipation during the last 21 ka for semidiurnal tides (blue) and diurnal tides (red), where the individual shadings represent the dissipation by $M_2$, $S_2$, $N_2 + K_2$ and $K_1$, $O_1$, $P_1 + Q_1$, respectively. Dissipation for diurnal and semidiurnal tidal species is presented on different scales. Further, the dissipation fraction by wave drag, $w_f$, for $M_2$ and $K_1$ (black, dashed/dashed-dotted), and the shelf-area fraction, $s_f$ (cyan-shaded) are superimposed. Additionally, the regimes *I* to *IV* that mark the change in stratification parameters employed for performing tidal simulations are overlaid (▷/◁: solutions in two neighboring regimes). The ●-markers present solutions obtained by employing an ice cover polewards of |45|°.

The most pronounced change in the global $M_2$-resonance is also related to this region. Mainly due to the blocking of the Hudson Straight and the global sea level drop, the North Atlantic $M_2$ amplitude is strongly amplified at 10 ka BP and earlier (Wilmes & Green, 2014; Haigh et al., 2020). The $M_2$-dissipation reaches a level of around 3.4–3.6 TW persisting approximately from 10.5 ka BP to the LGM. While the large-scale North Atlantic amphidromic system is responsible for the prominent increase in $M_2$ dissipation by 1 TW, several more localized resonances are observed, of which the transition of the Arctic tidal regime from micro-tidal to mega-tidal between 11.5 and 15.5 ka BP is the most prominent. The described changes also map to an increase in tidal levels, for example, HAT, that are displayed in Figures 6–8.

We further compare the predicted deep ocean dissipation under glacial conditions of this study to the findings of several recent studies, namely Wilmes and Green (2014); Wilmes et al. (2019), denoted W14 and W19, Velay-Vitow et al. (2020), denoted VV20, and Griffiths and Peltier (2008, 2009), denoted GP09. All studies predict a general increase in tidal dissipation, which is most prominent for $M_2$, and shifted toward dissipation by internal tide generation, that is, wave drag, which carries out approximately 60%–70% of the dissipation. This study predicts enhancement of wave drag dissipation by a factor of 2.4 (W19: 1.8–3; W14: 3–3.5; VV20: 1.4; GP09: 2.4). W19 computes the indicated range from variations of the Antarctic grounding line position, where paleo bathymetries derived from ICE5G and ICE6G result in a dissipation difference of 0.9 TW. Our predic-



**Figure 6.** Relative change of the HAT with respect to the present-day tidal range (0 ka BP) for selected time slices in cm. Regions of interest include the Atlantic Ocean, the Arctic Ocean, and the Caribbean Sea.

tions appear amid this estimate (similar to GP09). However, this study and GP09 consider the Arctic resonance ("Arctic Megatides," compare the following section), which was computationally supressed in W19 and W14. It is reasonable to assume that the Arctic resonance enhances Atlantic deep ocean dissipation and would presumably increase the dissipation estimates of W19. Thus, the dissipation estimates in this study would be closer to the lower boundary predicted by W19, obtained with ICE-6G.

The dissipation by diurnal tides changes only slightly but continuously with time. Even more, a weakly negative trend in the $K_1$-dissipation, also predicted by W14, VV20, and GP09, is overcompensated by a positive trend in the $O_1$-dissipation rate toward the LGM even though the tide-generating forces for $O_1$ are approximately 30% weaker than for $K_1$. Similar to this, VV20 finds an overall increase in the global and the deep ocean dissipation of $O_1$ (+25%), but to a smaller extent than in this article (+250%). In contrast to W14 and VV20, which estimate the glacial deep ocean dissipation fraction by diurnal tides to approximately 40%–60%, this study only predicts approximately 30% related to different parameterizations of topographic wave drag. $O_1$ becomes the most effective contributor to diurnal dissipation during the LGM, increasing the overall diurnal dissipation from 575 GW at present-day to 675 GW under LGM conditions. This large-scale $O_1$-resonance in the Pacific Ocean is accompanied by several shelf resonances, most notably in the South China Sea (cf. Figure 9).

The generally increased deep ocean dissipation is ultimately a consequence of the decreasing shelf sea fraction $s_f$ to values around 8%, resulting in blocking of Hudson Straight and drying-out of the Siberian shelf and large parts of the European shelf. This development removes these areas as energy sinks by turbulent bottom friction. Additionally, the emergence of the described shelf resonances, for example, in Hudson Bay, can have implications for global ocean dissipation. As shelf resonances tend to decrease the ocean tide amplitude in the coupled deep ocean, especially if they exhibit only weak frictional forces (Arbic & Garrett, 2010; Arbic et al., 2008). Thus, they can decrease the amount of energy dissipated by internal waves in the nearby deep ocean. This might be different for the Arctic resonance, that takes place in the deep ocean, basically altering the resonance conditions of the Atlantic Ocean as a whole.

We performed additional simulations to quantify the impact of an exuberant sea ice cover (polewards of $|\varphi| = 45°$) and report a minor impact on the observed dissipation pattern. We follow the reasoning that a decreased shelf area fraction $s_f$ minimizes the dissipation by turbulent bottom friction, which also applies to turbulent ice friction (i.e., doubled bottom friction). Both effects can only represent an efficient energy sink in shallow shelf areas that exhibit large barotropic current velocities, which are very sparse under glacial conditions (cf. Figure 5).

As the ocean stratification was changed between regimes *I* to *IV*, simulations at regime boundaries (0.5, 7.5, 18.5 ka BP) are repeated with wave drag tensors based on both regimes to quantify the impact of the ocean stratification on the simulation outcome. Figure 5 shows that, while $w_f$ can be affected by this parameter, the overall dissipation remains almost constant. In line with the results of Griffiths and Peltier (2009), this finding suggests that stratification changes are significant for baroclinic processes while the here discussed global barotropic tidal dynamics are pretty robust to changes in this parameter: Critical transitions of the tidal regime are triggered by bathymetric changes and the resulting resonance conditions and too far smaller extent by dissipation channels like wave drag or sea ice friction.

### 4.2. Tidal Levels

The following discussion relates to Figures 6–9 and exemplary focuses on the temporal evolution of the Highest Astronomical Tide, HAT. Changes in other tidal levels are found to be similar in character and are therefore not presented in detail. Please also consider Figures S2 to S9 in Supporting Information S1.

In line with the results of prior paleotidal studies (e.g., Thomas & Sündermann, 1999; Egbert et al., 2004; Wilmes & Green, 2014) we find that the most significant global-scale change of tidal levels is driven by the North Atlantic $M_2$-resonance, which is related to blocking of the Hudson Straight (Arbic, Garner, et al., 2004; Uehara et al., 2006). Setting in around 10 ka BP and before, the absolute value of the tidal levels strongly increases in most coastal regions of the North Atlantic. The increase is non-uniform, with hot spots reaching over +700 cm (e.g., Baffin Bay) and regions where even a slight decrease can be reported (e.g., the zone from Newfoundland to the Cap Verde Archipelago). Marginal seas are affected in different ways. While tidal amplitudes in the Mediterranean and the Baltic Sea remain small, prominent increases are observed for the Caribbean Sea up to +200 cm under LGM conditions (cf. Figure 9, bottom) and the Hudson Bay (cf. Figure 8, bottom), where tidal levels peak at 4.5 and 8 ka

BP due to an increased sea level before falling dry at 9–10 ka BP. On the other hand, $K_1$ exhibits similar global resonance characteristics under present-day and glacial conditions, except for an increased amplitude around Antarctica that is counterbalanced by a slight decrease of tidal amplitudes in other oceans (cf. Figure S5 in Supporting Information S1), as reported by other studies (e.g., Griffiths & Peltier, 2009; Wilmes & Green, 2014). Accompanying the increase of global $O_1$ dissipation (cf. Figure 5) we report increases in global $O_1$ amplitudes, especially in the Pacific Ocean, with even larger impacts on tidal levels in Pacific marginal Seas (cf. Figure S3 in Supporting Information S1). While the $S_2$ amplitudes increase in the North Atlantic similar to $M_2$, a reduction in the Pacific Ocean is predicted, which is the main driver of the HAT-drop at the North American West Coast under glacial conditions.

Another intriguing development is proposed for the White Sea (cf. Figure 8, top). The reduced sea level promotes the isolation of the respective basin between 9 and 13 ka BP, which causes HAT to drop close to zero. At the same time, the level at the nearby Barents Sea is elevated by over +350 cm. Interestingly this isolation only appears for the most recent bathymetry RTopo-2, whereas ETOPO5 or ETOPO2 (e.g., Amante & Eakins, 2009) show a deep channel on the western flank of the outlet, excluding isolation.

The most remarkable change is predicted for the Arctic Ocean. While the present-day tidal regime can be described as micro-tidal, several studies predict the transition to a mega-tidal regime under glacial conditions (Griffiths & Peltier, 2008, 2009; Velay-Vitow & Peltier, 2020; Velay-Vitow et al., 2020). While some tidal models employed for studying paleo-tides exclude a fully-unconstrained development of Arctic tides (e.g., Egbert et al., 2004), the rotated-pole numerical grid of TiME is well suited for studies of this region. In agreement with the findings of Velay-Vitow and Peltier (2020), a strong increase in tidal levels—mainly driven by the $M_2$ and $N_2$ tide (cf. Figures S6 to S9 in Supporting Information S1)—is predicted between the B/A and LGM. On the other hand, the predicted Arctic $M_2$ amplitude increase within this study is approximately 30% smaller than reported by VV20. This difference originates from the representation of SAL, which was parameterized as $\zeta_{SAL} = 0.085\zeta$ by VV20; considering the same local SAL implementation, we found an equivalent increase in the Arctic $M_2$ amplitude when considering the same implementation. This finding suggests a high sensitivity of the Arctic tide to the implementation of SAL, so that further studying this phenomenon is highly recommended.

Further changes in tidal levels in other world regions are predicted as well. The most substantial increases in HAT are found in several semi-enclosed basins developing around the Indonesian Archipelago while the sea level is falling (cf. Figure 9, top), for example, in the South China Sea by up to +250 cm. In this region the increase is caused by $K_1$ and even more by $O_1$, in line with the findings of Griffiths and Peltier (2009) and Uehara et al. (2006). On the other hand, the resonances in the Banda and the Coral Sea are caused and dominated by the semi-diurnal $M_2$-tide. Other basins experiencing smaller changes are, for example, the Patagonian shelf and the Seas around New Zealand (not shown), as well as the Caribbean Sea (cf. Figure 9, bottom). The latter was investigated by Hill et al. (2011), who found tidal levels rising from 7 ka BP by up to a factor of 2 at 10 ka BP which agrees with this study. A further local maximum at 9 ka BP (up to a factor of 3), we could not reproduce with TiME. The presented results can also be compared to the study by Ward et al. (2016), who investigated the European Shelf region, showing a good qualitative agreement. For instance, both studies predict an increased $M_2$-amplitude up to 400 cm at the coast of Brittany under glacial conditions, with a reduced amplitude of only 100 cm south of Ireland and in the Irish Sea (cf. Figure 9).

A notable special case is the Sea of Japan (cf. Figure 7). While this Sea is micro-tidal under present-day conditions, the glacially-induced GMSL drop isolates it even stronger from the deep ocean, leading to a considerable drop in the tidal levels. As previously mentioned, a larger source of uncertainty remains the position of the Antarctic grounding line. Therefore, the predicted increases in HAT in the Weddell Sea of up to +200 cm should be considered with caution.

## 5. Conclusion

We have applied the barotropic ocean model TiME (Sulzbach et al., 2021) to paleo topographic conditions from the Last Glacial Maximum to the present day. To investigate the impact of temporal changes of the ocean state on tidal dynamics, we discussed deviations in ocean stratification, sea-ice dynamics, and the geometry of ocean basins, that is, changes in bathymetry and shoreline position. We identified paleo bathymetry being the dominant factor, whereas ocean stratification and sea ice only marginally impact tidal amplitudes (e.g., Griffiths & Peltier, 2009). We also show that at a moderately high global resolution of $\frac{1}{6}^{\circ}$ (about 18.5 km), the tidal model agrees on a 70% level with present-day tide gauge data. As TiME is a data-unconstrained model, it can be applied directly to paleo topographies
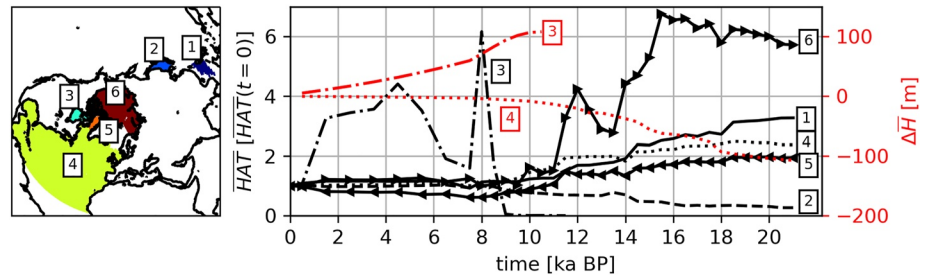
**Figure 7.** Development of the spatially averaged highest astronomical tide, $\overline{HAT}$, with respect to the present-day value, $\overline{HAT}(t=0)$ for several regions: South China Sea (1), Sea of Japan (2), Hudson Bay (3), North Atlantic (4), Baffin Bay (5) and the Arctic Ocean (6). The development of the mean depth $\overline{H}$ with respect to its modern value for (3) and (4) is shown, denoted $\Delta\overline{H}$. Please note that this value is not identical to $\overline{\Delta H}$, which is larger in Hudson Bay due to the variable shoreline.

and allows to reconstruct paleotidal conditions consistently. Furthermore, in TiME the spatial coordinate system can be rotated, allowing adjustment of the setup to a specific region of interest. In this study, a configuration was chosen, so that the North Atlantic and the Arctic Ocean are located in the center of the numerical domain, where the aspect ratio of the grid cells varies only slightly. Similar setups are possible for other regions of interest, for example, East Asia. In addition to this truly-global domain, comparable to Griffiths and Peltier (2008) and Velay-Vitow et al. (2020), TiME considers the non-local effect of SAL, formerly solitarily implemented for the deep-time simulations of Daher et al. (2021) and in the global model for glacial-interglacial cycles of Hill et al. (2011), but with a much coarser resolution of approximately $\frac{1}{2}^\circ$. Additional technical novelties in paleo ocean tide modeling are the wave drag scheme of Nycander (2005) and ice friction, which nevertheless had a minor impact on the simulation results.

Applying it to paleo topographies derived from ICE7G and the present-day RTopo-2 bathymetry, a combination that has not been investigated before, we obtain tidal amplitude changes of the main partial tides, and also derive tidal levels which are of importance for the interpretation of sea level data such as SLIPs. The novelty of the presented model can be summarized as simulating 4 partial tides and augmenting the results with 4 additional tides utilizing linear admittance theory and deriving tidal levels in the HOLSEA format. The constructed data set thus can be directly applied to study paleo sea level changes, see below.

The sea level was much lower during the Pleistocene. Accordingly, the tidal levels are expected to be larger due to less flooded continental shelves where the shallow waters serve as an efficient damping mechanism for ocean tide amplitudes, which has been repeatedly reported by prior paleotidal studies. Hence, in agreement to the findings of for example, Egbert et al. (2004); Griffiths and Peltier (2009); Wilmes et al. (2019); Velay-Vitow et al. (2020), the simulations predict a strong increase in semidiurnal deep ocean dissipation by internal tide generation. The here-reported dissipation rates lie in the span of former predictions. As especially $M_2$ is very sensitive to minor changes in the Antarctic paleo
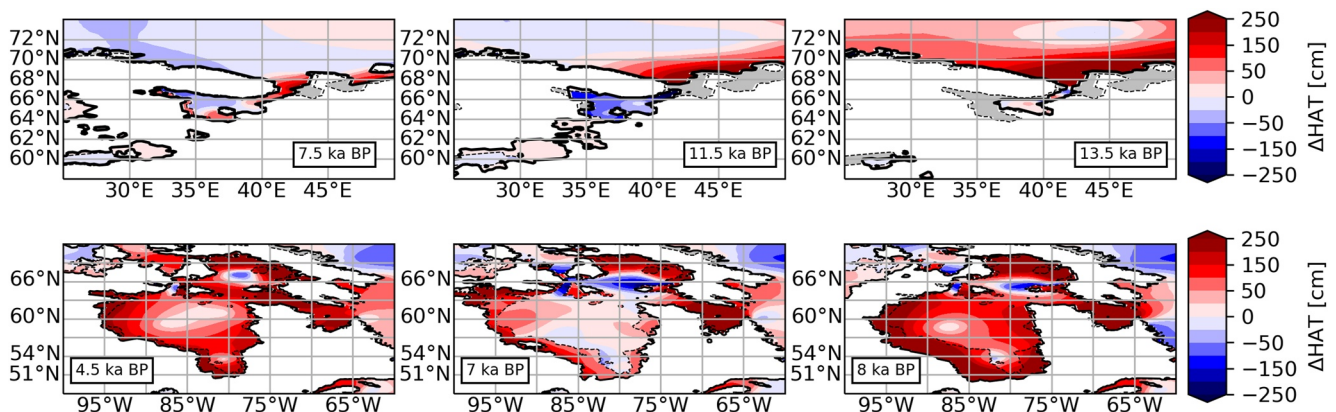


**Figure 8.** Changes in the highest astronomical tide (HAT) for selected time slices for the White Sea (top) and Hudson Bay (bottom) with respect to present-day conditions. Changes in the coastline are indicated by the dashed (present-day) and solid (contemporary) lines, with differences of the land mask in gray shading.

**Figure 9.** Changes in the highest astronomical tide (HAT) for selected time slices for the Indonesian Archipelago (top) and Caribbean Sea (bottom). Changes in the coastline are indicated by the dashed (present-day) and solid (contemporary) lines, with differences of the land mask in gray shading.
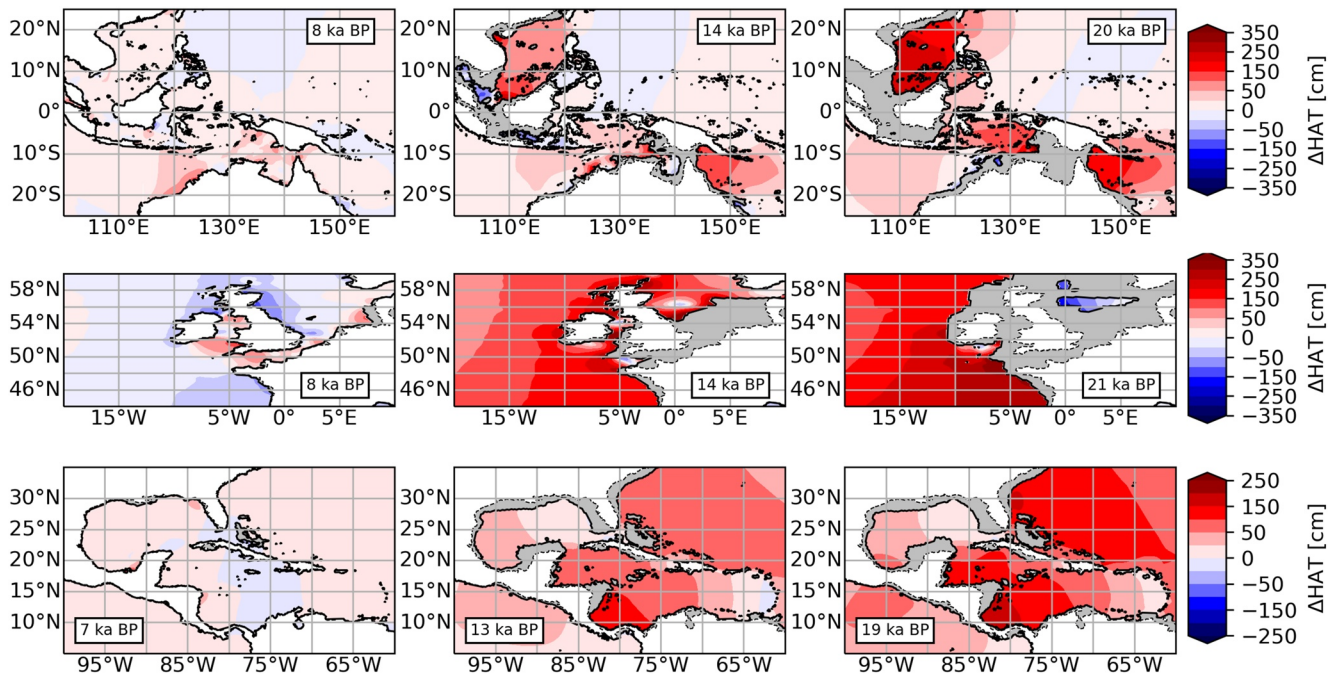
bathymetry (Wilmes & Green, 2014; Wilmes et al., 2019), the provided dissipation rates are afflicted with considerable uncertainty, which also maps to the tidal levels to a restricted degree, that is, tidal levels on the Northern hemisphere are more robust than close to Antarctica. Nonetheless, the provided data set allows us to reconstruct the temporal development of the deep ocean dissipation, which can be used to constrained paleo climate simulations (e.g., Green et al., 2009; Schmittner et al., 2015; Wilmes et al., 2019). A formerly not-discussed change is related to the $O_1$ tide, which is shifted toward a resonant state and becomes the main diurnal dissipator under glacial conditions.

Comparison to prior studies of paleotidal levels shows convincing qualitative agreement in most cases (Section 4.2). Yet, deviations from prior studies are found in some cases (e.g., North American East Coast, Arctic tides). An interesting open question remains the back action of the Arctic $M_2$-resonance on the abyssal dissipation in the North Atlantic with impacts on ocean mixing and the general circulation. While this study proposes a minor magnitude of this effect compared to changes in global $M_2$-resonance conditions, the local effect could be stronger pronounced. This secondary effect could be quantified within a future study where only the Arctic bathymetry is modified while keeping global conditions constant and observing changes in the basin-wise deep ocean dissipation for individual time slices. In addition to glacial resonances discussed in prior studies (e.g., North Atlantic, Arctic Ocean, South China Sea, Antarctic Kelvin wave), several new features are predicted by the global model. For instance, for the Atlantic region (cf. Figure 8), we found a Holocene high-tide episode around 5 ka BP for the Hudson Bay preceded by a further episode after deglaciation of this region around 8 ka BP. The White Sea shows diminishing tidal amplitudes around 11.5 ka BP due to isolation from the Barents Sea, when applying the most recent RTopo-2 bathymetry data set. In contrast, previous bathymetries showing deeper waters east of the Kola Peninsula do not support the isolation of the White Sea. In the tropical regions (cf. Figure 9), the separation of the Pacific from the Indian Ocean around 11 ka BP, resulted in the emergence of resonant conditions with a tidal level increase of 2–3 m in the South China Sea (e.g., Griffiths & Peltier, 2008), as well as in the Banda Sea and Coral Sea southwest and southeast of Java, respectively. These appear despite the fact that the semidiurnal tides of the open Pacific are only weakly affected by the paleo conditions (strongest reduction for $S_2$), but instead are related to the near-resonant conditions of the Pacific $O_1$-tide. Another curious example is the Sea of Japan, where tidal levels further decrease under glacial conditions.

A scan of all regional patterns of tidal changes is, of course, beyond the scope of this study, and—as shown for the White Sea—also depends critically on the applied bathymetry. Moreover, a higher spatial resolution is likely necessary to represent specific basin geometries more realistically. Nevertheless, the data underlying this article allows the closer inspection of arbitrary regions of interest in order to investigate their paleotidal dynamics and resulting
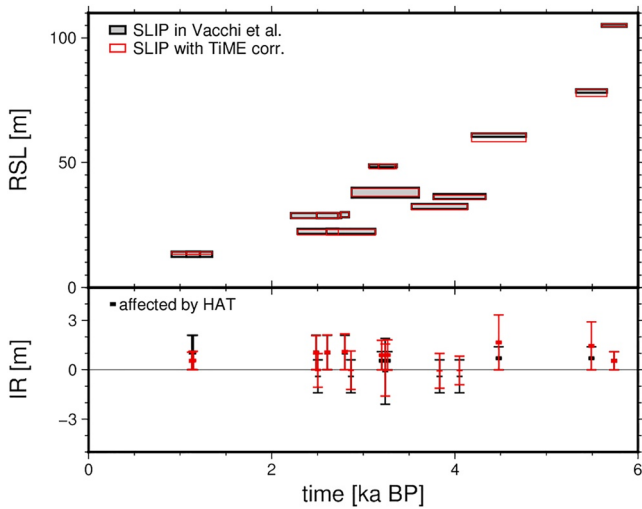
**Figure 10.** Relative sea level (RSL) and indicative range (IR) of SLIPs from the Hudson Bay. Top: RSL inferred from specific SLIPs; bottom: corresponding IR. Values published in Vacchi et al. (2018) (black), values determined with TiME (red). Error boxes at top are specified only by IR and dating of the SLIP.

tidal levels. We hypothesize that temporal differences in tidal levels, as presented in the figures, are likely to partially absorb residual modeling errors and should thus be considered in combination with a modern data-constrained tidal model (e.g., Egbert & Erofeeva, 2002; Hart-Davis, Piccioni, et al., 2021; Lyard et al., 2021) for maximum accuracy when interpreting SLIPs.

Accordingly, we provide the governing partial tides and the derived tidal levels for different time slices during the last deglaciation. These can be applied easily for further investigations. The tidal levels can directly be used to provide consistent paleotidal levels for Pleistocene and Holocene sea level data which are necessary to derive the indicative meaning and ranges of respective sample types. The partial tides allow to derive further tidal levels of interest or to investigate the tidal dynamics in specific regions. As partial tide solutions are provided (including tidal transports), they can be used to force regional paleotidal models (e.g., Hill et al., 2011), or can be included into baroclinic models, which are for example used to study climate or sedimentation (Drinkorn et al., 2021). All data is publicly accessible via doi https://doi.org/10.5880/GFZ.1.3.2022.005.

As a brief example of how the TiME-based paleotidal levels can contribute to discussions of SLIPs, we apply TiME to samples published in Vacchi et al. (2018). In Figure 10, SLIPs of the Hudson Bay between 6 ka BP and present day are presented, for which tidal levels specify the indicative range (IR). However, samples specified by MTL only and those from gravel beaches, where a constant storm-beach correction of 3 m was added, were excluded (for details, see Vacchi et al. (2018), Table 1). For the remaining SLIPs, RSL and IR presented in Vacchi et al. (2018) are compared with those, where the tidal ranges predicted with TiME are considered.

The Hudson Bay is located in a region of post-glacial uplift. Accordingly, we observe already during the last 6 ka a significant RSL fall of more than 100 m and the differences in RSL due to deviations in the considered tidal levels appear to be small. In the compilation of Vacchi et al. (2018), the paleotidal model of Hill et al. (2011) was applied, which covers the western North Atlantic, but not the Arctic. Accordingly, the authors did not consider deviations from modern tidal levels for SLIPs of the Hudson Bay. For all samples the IR is specified by two tidal levels. For instance, the tidal range between MTL and HAT defines the IR of macrofossils representing intertidal facies, marked as box-symbols in the lower plot of Figure 10. In general, The IR shows a good agreement between the two tidal correction models. It is evident that the IR predicted by TiME increases with time due to larger tidal levels (see also Figure 7) and so is significantly larger than the values of Vacchi et al. (2018). As the IR is usually considered as an uncertainty (e.g., Khan et al., 2017), these changes influence the statistical analysis of paleo sea level change in this region.

As a final note, the flexibility of the tidal model TiME allows for further increasing the tidal solution's spatial resolution. This can be met by utilizing a well-tested configuration with $\frac{1}{12}^{\circ}$ horizontal grid sampling (Sulzbach et al., 2021), or experimental setups with even higher resolution. Reaching the 10 km resolution level reduces the need to employ regional numerical models, which are both computationally expensive and challenging to implement due to the need for consistent flow data at the open boundaries.

## Appendix A: Estimating Spring/Neap Tide Levels

To derive estimates for the spring/neap-cycle related parameters MLWS, MHWS, MLWN, and MHWN from the given set of eight partial tides, we employ the auxiliary functions

$$p_{\pm} = \frac{f_{\pm}\left(A_{\mathrm{mod}}^{\mathrm{O_1}}, A_{\mathrm{mod}}^{\mathrm{K_1}}\right)\sqrt{\left(A_{\mathrm{mod}}^{\mathrm{K_1}}\right)^2 + \left(A_{\mathrm{mod}}^{\mathrm{O_1}}\right)^2} + f_{\pm}\left(A_{\mathrm{mod}}^{\mathrm{S_2}}, A_{\mathrm{mod}}^{\mathrm{M_2}}\right)\sqrt{\left(A_{\mathrm{mod}}^{\mathrm{S_2}}\right)^2 + \left(A_{\mathrm{mod}}^{\mathrm{M_2}}\right)^2}}{\sqrt{\left(A_{\mathrm{mod}}^{\mathrm{K_1}}\right)^2 + \left(A_{\mathrm{mod}}^{\mathrm{O_1}}\right)^2} + \sqrt{\left(A_{\mathrm{mod}}^{\mathrm{S_2}}\right)^2 + \left(A_{\mathrm{mod}}^{\mathrm{M_2}}\right)^2}} \tag{A1}$$

with $f_{\pm}(a, b) = |a \pm b|/\max(a, b)$. These dimensionless factors ($\pm$: spring/neap) fulfill the condition $0 \leq p_- \leq 1 \leq p_+ \leq 2$. To estimate the spring tide modification, we weigh the maximum possible constructive

interference, $|a + b|$ of the two dominant partial tides per band ($M_2$ and $S_2$ vs. $O_1$ and $K_1$) with the respective mean quadratic amplitude per tidal band. Correspondingly, the respective neap tide values relate to the minimum possible amplitude through destructive interference $|a - b|$.

## Appendix B: Linear Admittance Assumptions for Tidal Dissipation

The mean energy dissipation $\overline{D}_i$ by a certain partial tide $i$ equals the respective mean tidal energy consumption and can be estimated by the global integral

$$\overline{D}_i = \rho_{\mathrm{sw}} \int dA \, \overline{\boldsymbol{\nabla}\phi_{\mathrm{tid}}^i(\boldsymbol{x}, \omega_i t) \cdot \mathbf{V}^i(\boldsymbol{x}, \omega_i t)}, \tag{B1}$$

where $\mathbf{V}^i = H \, \mathbf{v}^i$ is the tidal transport and $\phi_{\mathrm{tid}}^i$ is the respective partial tide generating potential. We only consider partial tides of second degree as the energy dissipation of higher-degree tides (e.g., degree-3) is negligible ($\ll$ 1 GW) (Sulzbach, Wziontek, et al., 2022). Thus, we set

$$\phi_{\mathrm{tid}}^i(\boldsymbol{x}, \omega_i t) = \alpha_2(\omega_i) \, A_i \, (Y_{2m}(\boldsymbol{x}) \cos(\omega_i t) - Y_{2-m}(\boldsymbol{x}) \sin(\omega_i t)) \tag{B2}$$

introducing the factor $\alpha_2(\omega_i) = 1 + k_2(\omega_i) - h_2(\omega_i)$, which is a combination of body tide Love numbers, the amplitude factor $A_i(\omega_i)$ and the real-valued, fully-normalized spherical harmonic functions $Y_{lm}(\boldsymbol{x})$ as defined in Heiskanen and Moritz (1967). Please note that $\alpha_2(\omega_i)$ is a frequency-dependent factor due to the NDFW-resonance and experiences considerable variations for some diurnal tides (e.g., $K_1$). Further, we assume linear admittance of the tidal velocities $\mathbf{v}^i$ setting

$$\mathbf{v}^i(\boldsymbol{x}, \omega_i t) = A_i \, \alpha_2(\omega_i) \Big[ \big(\mathbf{v}_0^{\cos}(\boldsymbol{x}) + \mathbf{v}_1^{\cos}(\boldsymbol{x}) \, \omega_i\big) \cos \omega_i t + \big(\mathbf{v}_0^{\sin}(\boldsymbol{x}) + \mathbf{v}_1^{\sin}(\boldsymbol{x}) \, \omega_i\big) \sin \omega_i t \Big] . \tag{B3}$$

Employing the latter equations, the mean energy dissipation in Eq. (B1) can be calculated. This results in Equation 4, which is then fitted to the data points obtained from $M_2$, $K_2$, $O_1$, and $K_1$. While this 2-point evaluation per tidal band helps to sharpen the image of global tidal dissipation, it increases the uncertainty of the obtained result, as admittance is only approximately linear. The precision of this result can be improved by simulating more partial tides and considering a piece-wise steady approximation of the admittance function. Within the current approach, $Q_1$ and $N_2$ inherit the largest uncertainty, as they possess the most prominent frequency difference from the simulated tides.

## Data Availability Statement

The modeling data discussed in this paper are published separately at Sulzbach, Klemann, Dobslaw, and Thomas (2022). We provide tidal levels and the temporal evolution of tidal dissipation in NetCDF format. Further, the individual partial tide solutions for all directly simulated tides are included. They can provide open boundary conditions for regional paleotidal simulations or can be employed to derive other statistical observables of tidal dynamics. The data are provided on the employed rotated-pole grid and supplemented by a routine to project the data to standard longitude-latitude coordinates. Graphics were created with Inkscape (Inkscape Project, 2020). Plots were generated with matplotlib (Hunter, 2007), cartopy (Met Office, 2010 - 2015) and gmt6 (Wessel et al., 2019), while data processing was done applying the software package numpy (Harris et al., 2020). This study used the FES2014 tidal atlas, which was produced by Novelties, Legos and CLS and distributed by Aviso+ with support from CNES (Lyard et al., 2021).

## References

Abe-Ouchi, A., Saito, F., Kawamura, K., Raymo, M. E., Okuno, J., Takahashi, K., & Blatter, H. (2013). Insolation-driven 100,000-year glacial cycles and hysteresis of ice-sheet volume. *Nature*, *500*(7461), 190–193. https://doi.org/10.1038/nature12374

Accad, Y., & Pekeris, C. L. (1978). Solution of the tidal equations for the M2 and S2 tides in the world oceans from a knowledge of the tidal potential alone. *Philosophical Transactions of the Royal Society of London, Series A*, *290*, 235–266. https://doi.org/10.1098/rsta.1978.0083

Amante, C., & Eakins, B. (2009). ETOPO1 1 arc-minute global relief model: Procedures, data sources and analysis. In *NOAA technical memorandum NESDIS NGDC-24*. National Geophysical Data Center, NOAA. https://doi.org/10.7289/V5C8276M

Arbic, B. K., Garner, S. T., Hallberg, R. W., & Simmons, H. L. (2004). The accuracy of surface elevations in forward global barotropic and baroclinic tide models. *Deep Sea Research Part II: Topical Studies in Oceanography*, *51*(25–26), 3069–3101. https://doi.org/10.1016/j.dsr2.2004.09.014

Arbic, B. K., & Garrett, C. (2010). A coupled oscillator model of shelf and ocean tides. *Continental Shelf Research*, *30*(6), 564–574. https://doi.org/10.1016/j.csr.2009.07.008

Arbic, B. K., MacAyeal, D. R., Mitrovica, J. X., & Milne, G. A. (2004). Ocean tides and Heinrich events. *Nature*, *432*(7016), 460. https://doi.org/10.1038/432460a

Arbic, B. K., Mitrovica, J. X., MacAyeal, D. R., & Milne, G. A. (2008). On the factors behind large Labrador Sea tides during the last glacial cycle and the potential implications for Heinrich events. *Paleoceanography*, *23*(3), 1–14. https://doi.org/10.1029/2007PA001573

Arbic, B. K., St.-Laurent, P., Sutherland, G., & Garrett, C. (2007). On the resonance and influence of the tides in Ungava Bay and Hudson Strait. *Geophysical Research Letters*, *34*, 1–7. https://doi.org/10.1029/2007GL030845

Barnett, R. L., Charman, D. J., Johns, C., Ward, S. L., Bevan, A., Bradley, S. L., et al. (2020). Nonlinear landscape and cultural response to sea-level rise. *Science Advances*, *6*(45), eabb6376. https://doi.org/10.1126/sciadv.abb6376

Bell, T. H. (1975). Topographically generated internal waves in the open ocean. *Journal of Geophysical Research*, *80*(3), 320–327. https://doi.org/10.1029/jc080i003p00320

Berends, C. J., de Boer, B., & van de Wal, R. S. W. (2021). Reconstructing the evolution of ice sheets, sea level, and atmospheric $CO_2$ during the past 3.6 million years. *Climate of the Past*, *17*(1), 361–377. https://doi.org/10.5194/cp-17-361-2021

Bij de Vaatie, I., Vasulkar, A. N., Slobbe, D. C., & Verlaan, M. (2021). The influence of Arctic landfast ice on seasonal modulation of the M2 tide. *Journal of Geophysical Research: Oceans*, *126*, e2020JC016630. https://doi.org/10.1029/2020JC016630

Bretagnon, P. (1982). Théorie du mouvement de l'ensemble des planètes. Solution VSOP82. *Astronomy & Astrophysics*, *114*, 278–288.

Briggs, R. D., & Tarasov, L. (2013). How to evaluate model-derived deglaciation chronologies: A case study using Antarctica. *Quaternary Science Reviews*, *63*, 109–127. https://doi.org/10.1016/j.quascirev.2012.11.021

Cancet, M., Andersen, O., Lyard, F., Schulz, A., Cotton, D., & Benveniste, J. (2016). *A new high resolution tidal model in the Arctic Ocean*. European Space Agency, (Special Publication) ESA SP. SP-740.

Cartwright, D. E. (1999). *Tides: A scientific history*. Cambridge University Press.

Clark, P. U., Shakun, J. D., Marcott, S. A., Mix, A. C., Eby, M., Kulp, S., et al. (2016). Consequences of twenty-first-century policy for multi-millennial climate and sea-level change. *Nature Climate Change*, *6*(4), 360–369. https://doi.org/10.1038/nclimate2923

CLIMAP-Project-Members (1981). *Map and Chart Ser. MC-36, Chap. Seasonal reconstruction of the Earth surface at the last glacial maximum*. Lamont-Doherty Geological Observatory of Columbia University. Retrieved from https://www.ncei.noaa.gov/access/paleo-search/study/2516

Cooper, J. A. G., Green, A. N., & Compton, J. S. (2018). Sea-level change in southern Africa since the Last Glacial Maximum. *Quaternary Science Reviews*, *201*, 303–318. https://doi.org/10.1016/j.quascirev.2018.10.013

Daher, H., Arbic, B. K., Williams, J. G., Ansong, J. K., Boggs, D. H., Müller, M., et al. (2021). Long-term Earth-Moon evolution with high-level orbit and ocean tide models. *Journal of Geophysical Research: Planets*, *126*(12), 1–39. https://doi.org/10.1029/2021JE006875

Davies, H. S., Green, J. A. M., & Duarte, J. C. (2020). Back to the future II: Tidal evolution of four supercontinent scenarios. *Earth System Dynamics*, *11*(1), 291–299. https://doi.org/10.5194/esd-11-291-2020

Doodson, A. T. (1921). The harmonic development of the tide-generating potential. *Proceedings of the Royal Society of London*, *100*, 305–329. https://doi.org/10.1098/rspa.1921.0088

Drinkorn, C., Saynisch-wagner, J., Uenzelmann-neben, G., & Thomas, M. (2021). Decadal climate sensitivity of contouritic sedimentation in a dynamically coupled ice-ocean-sediment model of the North Atlantic. *Palaeogeography, Palaeoclimatology, Palaeoecology*, *572*, 110391. https://doi.org/10.1016/j.palaeo.2021.110391

Egbert, G. D., & Erofeeva, S. Y. (2002). Efficient inverse modeling of Barotropic Ocean tides. *Journal of Atmospheric and Oceanic Technology*, *19*(2), 183–204. https://doi.org/10.1175/1520-0426(2002)019⟨0183:EIMOBO⟩2.0.CO;2

Egbert, G. D., & Ray, R. D. (2000). Significant dissipation of tidal energy in the deep ocean inferred from satellite altimeter data. *Nature*, *405*(6788), 775–778. https://doi.org/10.1038/35015531

Egbert, G. D., & Ray, R. D. (2001). Estimates of M2 tidal energy dissipation from TOPEX/Poseidon altimeter data. *Journal of Geophysical Research*, *106*(C10), 22475–22502. https://doi.org/10.1029/2000jc000699

Egbert, G. D., Ray, R. D., & Bills, B. G. (2004). Numerical modeling of the global semidiurnal tide in the present day and in the Last Glacial Maximum. *Journal of Geophysical Research*, *109*(C3), 1–15. https://doi.org/10.1029/2003jc001973

Garrett, E., Melnick, D., Dura, T., Cisternas, M., Ely, L. L., Wesson, R. L., et al. (2020). Holocene relative sea-level change along the tectonically active Chilean coast. *Quaternary Science Reviews*, *236*, 106281. https://doi.org/10.1016/j.quascirev.2020.106281

Green, J. A. M. (2010). Ocean tides and resonance. *Ocean Dynamics*, *60*(5), 1243–1253. https://doi.org/10.1007/s10236-010-0331-1

Green, J. A. M., Green, C. L., Bigg, G. R., Rippeth, T. P., Scourse, J. D., & Uehara, K. (2009). Tidal mixing and the meridional overturning circulation from the Last Glacial Maximum. *Geophysical Research Letters*, *36*(15), L15603. https://doi.org/10.1029/2009GL039309

Green, J. A. M., Huber, M., Waltham, D., Buzan, J., & Wells, M. (2017). Explicitly modelled deep-time tidal dissipation and its implication for Lunar history. *Earth and Planetary Science Letters*, *461*, 46–53. https://doi.org/10.1016/j.epsl.2016.12.038

Griffiths, S. D., & Hill, D. F. (2015). Tidal modeling. In *Handbook of sea-level research* (pp. 438–451). John Wiley & Sons, Ltd. https://doi.org/10.1002/9781118452547.ch29

Griffiths, S. D., & Peltier, W. R. (2008). Megatides in the Arctic Ocean under glacial conditions. *Geophysical Research Letters*, *35*(8), 1–5. https://doi.org/10.1029/2008GL033263

Griffiths, S. D., & Peltier, W. R. (2009). Modeling of polar ocean tides at the Last Glacial Maximum: Amplification sensitivity, and climatological implications. *Journal of Climate*, *22*(11), 2905–2924. https://doi.org/10.1175/2008JCLI2540.1

Haigh, I. D., Pickering, M. D., Green, J. A., Arbic, B. K., Arns, A., Dangendorf, S., et al. (2020). The tides they are a-changing': A comprehensive review of past and future nonastronomical changes in tides, their driving mechanisms, and future implications. *Reviews of Geophysics*, *58*, 1–39. https://doi.org/10.1029/2018RG000636

Harris, C. R., Millman, K. J., van der Walt, S. J., Gommers, R., Virtanen, P., Cournapeau, D., et al. (2020). Array programming with NumPy. *Nature*, *585*(7825), 357–362. https://doi.org/10.1038/s41586-020-2649-2

Hart-Davis, M. G., Dettmering, D., Sulzbach, R., Thomas, M., Schwatke, C., & Seitz, F. (2021). Regional evaluation of minor tidal constituents for improved estimation of ocean tides. *Remote Sensing*, *13*(16), 3310. https://doi.org/10.3390/rs13163310

Hart-Davis, M. G., Piccioni, G., Dettmering, D., Schwatke, C., Passaro, M., & Seitz, F. (2021). EOT20: A global ocean tide model from multi-mission satellite altimetry. *Earth System Science Data Discussions*, 1–23. https://doi.org/10.5194/essd-2021-97

Hartmann, T., & Wenzel, H. (1994). The harmonic development of the Earth tide generating potential due to the direct effect of the planets. *Geophysical Research Letters*, *21*(18), 1991–1993. https://doi.org/10.1029/94GL01684

Hartmann, T., & Wenzel, H.-G. (1995). The HW95 tidal potential catalogue. *Geophysical Research Letters*, *22*(24), 3553–3556. https://doi.org/10.1029/95gl03324

Heiskanen, W. A., & Moritz, H. (1967). *Physical geodesy*. Springer Vienna. https://doi.org/10.1007/b139113

Hijma, M. P., Engelhart, S. E., Törnqvist, T. E., Horton, B. P., Hu, P., & Hill, D. F. (2015). A protocol for a geological sea-level database. In I. Shennan, A. J. Long, & B. P. Horton (Eds.), *Handbook of sea-level research* (pp. 536–553). John Wiley & Sons, Ltd. https://doi.org/10.1002/9781118452547.ch34

Hijma, M. P., & Cohen, K. M. (2019). Holocene sea-level database for the Rhine-Meuse Delta, The Netherlands: Implications for the pre-8.2 ka sea-level jump. *Quaternary Science Reviews*, *214*, 68–86. https://doi.org/10.1016/j.quascirev.2019.05.001

Hill, D. F., Griffiths, S. D., Peltier, W. R., Horton, B. P., & Törnqvist, T. E. (2011). High-resolution numerical modeling of tides in the western Atlantic, Gulf of Mexico, and Caribbean Sea during the Holocene. *Journal of Geophysical Research*, *116*(C10), C10014. https://doi.org/10.1029/2010JC006896

Hillenbrand, C.-D., Bentley, M. J., Stolldorf, T. D., Hein, A. S., Kuhn, G., Graham, A. G., et al. (2014). Reconstruction of changes in the Weddell Sea sector of the Antarctic Ice Sheet since the Last Glacial Maximum. *Quaternary Science Reviews*, *100*, 111–136. https://doi.org/10.1016/j.quascirev.2013.07.020

Horton, B. P., Engelhart, S. E., Hill, D. F., Kemp, A. C., Nikitina, D., Miller, K. G., & Peltier, W. R. (2013). Influence of tidal-range change and sediment compaction on Holocene relative sea-level change in New Jersey, USA. *Journal of Quaternary Science*, *28*(4), 403–411. https://doi.org/10.1002/jqs.2634

Howarth, M. J. (1998). The effect of stratification on tidal current profiles. *Continental Shelf Research*, *18*(11), 1235–1254. https://doi.org/10.1016/S0278-4343(98)00042-9

Hunter, J. D. (2007). Matplotlib: A 2D graphics environment. *Computing in Science & Engineering*, *9*(3), 90–95. https://doi.org/10.1109/MCSE.2007.55

Idier, D., Paris, F., Cozannet, G. L., Boulahya, F., & Dumas, F. (2017). Sea-level rise impacts on the tides of the European Shelf. *Continental Shelf Research*, *137*, 56–71. https://doi.org/10.1016/j.csr.2017.01.007

Inkscape Project. (2020). Inkscape [Software]. Inkscape. Retrieved from https://inkscape.org

IPCC. (2022). In H.-O. Pörtner, D. C. Roberts, M. Tignor, et al. (Eds.), *Climate Change 2022: Impacts, adaptation and vulnerability working group II contribution to the IPCC sixth assessment report citations to the sixth assessment report of the intergovernmental panel on climate change*. Cambridge University Press. https://doi.org/10.1017/9781009325844

Jakobsson, M., Andreassen, K., Bjarnadóttir, L. R., Dove, D., Dowdeswell, J. A., England, J. H., et al. (2014). Arctic Ocean glacial history. *Quaternary Science Reviews*, *92*, 40–67. https://doi.org/10.1016/j.quascirev.2013.07.033

Jungclaus, J. H., Lorenz, S. J., Timmreck, C., Reick, C. H., Brovkin, V., Six, K., et al. (2010). Climate and carbon-cycle variability over the last millennium. *Climate of the Past*, *6*(5), 723–737. https://doi.org/10.5194/cp-6-723-2010

Kagan, B. A., & Sofina, E. (2009). Ice-induced seasonal variability of tidal constants in the Arctic Ocean. *Continental Shelf Research*, *30*(6), 643–647. https://doi.org/10.1016/j.csr.2009.05.010

Kagan, B. A., & Sündermann, J. (1996). Dissipation of tidal energy, paleotides, and the evolution of the Earth-Noon system. *Advances in Geophysics*, *38*, 179–266. https://doi.org/10.1016/S0065-2687(08)60021-7

Khan, N. S., Ashe, E., Horton, B. P., Dutton, A., Kopp, R. E., Brocard, G., et al. (2017). Drivers of Holocene sea-level change in the Caribbean. *Quaternary Science Reviews*, *155*, 13–36. https://doi.org/10.1016/j.quascirev.2016.08.032

Khan, N. S., Horton, B. P., Engelhart, S., Rovere, A., Vacchi, M., HOLSEA Working Group, et al. (2019). Inception of a global atlas of sea levels since the Last Glacial Maximum. *Quaternary Science Reviews*, *220*, 359–371. https://doi.org/10.1016/j.quascirev.2019.07.016

Levitus, S. (2009). *NODC standard product: World Ocean Atlas 2009 (NCEI accession 0094866)*. US DOC/NOAA/NESDIS ¿ National Oceanographic Data Center (2013). NOAA National Centers for Environmental Information Retrieved from https://accession.nodc.noaa.gov/0094866

Llewellyn Smith, S. G., & Young, W. R. (2003). Tidal conversion at a very steep ridge. *Journal of Fluid Mechanics*, *495*, 175–191. https://doi.org/10.1017/S0022112003006098

Lyard, F. H., Allain, D. J., Cancet, M., Carrère, L., & Picot, N. (2021). FES2014 global ocean tide atlas: Design and performance. *Ocean Science*, *17*(3), 615–649. https://doi.org/10.5194/os-17-615-2021

Met Office. (2010–2015). Cartopy: A cartographic python library with a matplotlib interface. [Software]. Exeter, Devon Retrieved from http://scitools.org.uk/cartopy

Mignard, F. (1979). The evolution of the Lunar orbit revisited. *The Moon and the Planets*, *20*(3), 301–315. https://doi.org/10.1007/BF00907581

Müller, M. (2007). The free oscillations of the world ocean in the period range 8 to 165 hours including the full loading effect. *Geophysical Research Letters*, *34*, 1–5. https://doi.org/10.1029/2006GL028870

Müller, M., Cherniawsky, J. Y., Foreman, M. G., & Storch, J. S. V. (2014). Seasonal variation of the M2 tide. *Ocean Dynamics*, *64*(2), 159–177. https://doi.org/10.1007/s10236-013-0679-0

Müller, M., Haak, H., Jungclaus, J. H., Sündermann, J., & Thomas, M. (2010). The effect of ocean tides on a climate model simulation. *Ocean Modelling*, *35*(4), 304–313. https://doi.org/10.1016/j.ocemod.2010.09.001

Munk, W. H., & Cartwright, D. E. (1966). Tidal spectroscopy and prediction. *Philosophical Transactions of the Royal Society A: Mathematical, Physical & Engineering Sciences*, *259*, 533–581. https://doi.org/10.2307/j.ctt211qv60.7

Neill, S. P., Scourse, J. D., & Uehara, K. (2010). Evolution of bed shear stress distribution over the northwest European shelf seas during the last 12,000 years. *Ocean Dynamics*, *60*(5), 1139–1156. https://doi.org/10.1007/s10236-010-0313-3

Nycander, J. (2005). Generation of internal waves in the deep ocean by tides. *Journal of Geophysical Research*, *110*(C10), 1–9. https://doi.org/10.1029/2004JC002487

Peltier, W. R. (1994). Ice age paleotopography. *Science*, *265*(5169), 195–201. https://doi.org/10.1126/science.265.5169.195

Peng, D., Hill, E. M., Meltzner, A. J., & Switzer, A. D. (2019). Tide gauge records show that the 18.61-year nodal tidal cycle can change high water levels by up to 30 cm. *Journal of Geophysical Research: Oceans*, *124*(1), 736–749. https://doi.org/10.1029/2018JC014695

Petit, G., & Luzum, B. (2010). IERS conventions (2010). Bureau international des poids et mesures sevres (France) technical note No. 36. Retrieved from http://www.iers.org/TN36/

Piccioni, G., Dettmering, D., Bosch, W., & Seitz, F. (2019). Ticon: TIdal CONstants based on GESLA sea-level records from globally located tide gauges. *Geoscience Data Journal*, *6*(2), 97–104. https://doi.org/10.1002/gdj3.72

Ray, R. D. (1998). Ocean self-attraction and loading in numerical tidal models. *Marine Geodesy*, *21*(3), 181–192. https://doi.org/10.1080/01490419809388134

Ray, R. D. (2013). Precise comparisons of bottom-pressure and altimetric ocean tides. *Journal of Geophysical Research: Oceans*, *118*(9), 4570–4584. https://doi.org/10.1002/jgrc.20336

Ray, R. D., Eanes, R. J., & Lemoine, F. G. (2001). Constraints on energy dissipation in the Earth's body tide from satellite tracking and altimetry. *Geophysical Journal International*, *144*(2), 471–480. https://doi.org/10.1046/j.1365-246X.2001.00356.x

Rieser, D., Tr, T. M.-G., Savcenko, R., Bosch, W., Wünsch, J., Dahle, C., & Flechtner, F. (2012). The ocean tide model EOT11a in spherical harmonics representation. Technical Note. Retrieved from http://portal.tugraz.at/portal/page/portal/Files/i5210/files/projekte/COTAGA/TN_EOT11a.pdf

Roy, K., & Peltier, W. (2015). Glacial isostatic adjustment, relative sea level history and mantle viscosity: Reconciling relative sea level model predictions for the U.S. East Coast with geological constraints. *Geophysical Journal International*, *201*(2), 1156–1181. https://doi.org/10.1093/gji/ggv066

Roy, K., & Peltier, W. (2018). Relative sea level in the Western Mediterranean basin: A regional test of the ICE-7G-NA (VM7) model and a constraint on late Holocene Antarctic deglaciation. *Quaternary Science Reviews*, *183*, 76–87. https://doi.org/10.1016/j.quascirev.2017.12.021

Schaffer, J., Timmermann, R., Arndt, J. E., Kristensen, S. S., Mayer, C., Morlighem, M., & Steinhage, D. (2016). A global, high-resolution data set of ice sheet topography, cavity geometry, and ocean bathymetry. *Earth System Science Data*, *8*(2), 543–557. https://doi.org/10.5194/essd-8-543-2016

Schindelegger, M., Green, J. A., Wilmes, S. B., & Haigh, I. D. (2018). Can we model the effect of observed sea level rise on tides? *Journal of Geophysical Research: Oceans*, *112*(7), 95–110. https://doi.org/10.1029/2018JC013959

Schmittner, A., Green, J. A., & Wilmes, S. B. (2015). Glacial ocean overturning intensified by tidal mixing in a global circulation model. *Geophysical Research Letters*, *42*(10), 4014–4022. https://doi.org/10.1002/2015GL063561

Schrama, E. J., & Ray, R. D. (1994). A preliminary tidal analysis of TOPEX/POSEIDON altimetry. *Journal of Geophysical Research*, *99*(C12), 24799. https://doi.org/10.1029/94jc01432

Sejrup, H. P., Larsen, E., Landvik, J., King, E. L., Haflidason, H., & Nesje, A. (2000). Quaternary glaciations in southern Fennoscandia: Evidence from southwestern Norway and the northern North Sea region. *Quaternary Science Reviews*, *19*(7), 667–685. https://doi.org/10.1016/S0277-3791(99)00016-5

Simon, J. L., Bretagnon, P., Chapront, J., Chapront-Touzé, M., Francou, G., & Laskar, J. (1994). Numerical expressions for precession formulae and mean elements for the Moon and the planets. *Astronomy and Astrophysics*, *282*, 663–683.

Simon, K. M., James, T. S., Forbes, D. L., Telka, A. M., Dyke, A. S., & Henton, J. A. (2014). A relative sea-level history for Arviat, Nunavut, and implications for Laurentide ice sheet thickness west of Hudson Bay. *Quaternary Research (United States)*, *82*(1), 185–197. https://doi.org/10.1016/j.yqres.2014.04.002

Stammer, D., Ray, R. D., Andersen, O. B., Arbic, B. K., Bosch, W., Carrère, L., et al. (2014). Accuracy assessment of global barotropic ocean tide models. *Reviews of Geophysics*, *52*(3), 243–282. https://doi.org/10.1002/2014RG000450.Received

Stein, R., Fahl, K., Gierz, P., Frank Niessen, G. L., & Lohmann, G. (2017). Arctic Ocean sea ice cover during the penultimate glacial and the last interglacial. *Nature Communications*, *8*(1), 373. https://doi.org/10.1038/s41467

St. Laurent, L. C., Simmons, H. L., & Jayne, S. R. (2002). Estimating tidally driven mixing in the deep ocean. *Geophysical Research Letters*, *29*, 19–22. https://doi.org/10.1029/2002GL015633

Sulzbach, R., Dobslaw, H., & Thomas, M. (2021). High-resolution numerical modelling of barotropic global ocean tides for satellite gravimetry. *Journal of Geophysical Research: Oceans*, *126*(5), 1–21. https://doi.org/10.1029/2020JC017097

Sulzbach, R., Klemann, V., Dobslaw, H., & Thomas, M. (2022). Global ocean tide model data during the last 21,000 years [Dataset]. GFZ Data Services. https://doi.org/10.5880/GFZ.1.3.2022.005

Sulzbach, R., Wziontek, H., Hart-Davis, M. G., Dobslaw, H., Scherneck, H.-G., Camp, M. V., et al. (2022). Modeling gravimetric signatures of third-degree ocean tides and their detection in superconducting gravimeter records. *Journal of Geodesy*, *96*(5), 35. https://doi.org/10.1007/s00190-022-01609-w

Sun, Y., Knorr, G., Zhang, X., Tarasov, L., Barker, S., Werner, M., & Lohmann, G. (2022). Ice sheet decline and rising atmospheric CO2 control AMOC sensitivity to deglacial meltwater discharge. *Global and Planetary Change*, *210*, 103755. https://doi.org/10.1016/j.gloplacha.2022.103755

Tarasov, L., Dyke, A. S., Neal, R. M., & Peltier, W. R. (2012). A data-calibrated distribution of deglacial chronologies for the North American ice complex from glaciological modeling. *Earth and Planetary Science Letters*, *315*(316), 30–40. https://doi.org/10.1016/j.epsl.2011.09.010

Thomas, M., & Sündermann, J. (1999). Tides and tidal torques of the world ocean since the Last Glacial Maximum. *Journal of Geophysical Research*, *104*(C2), 3159–3183. https://doi.org/10.1029/1998JC900097

Tushingham, A. M., & Peltier, W. R. (1992). Validation of the ICE-3G Model of Würm-Wisconsin Deglaciation using a global data base of relative sea level histories. *Journal of Geophysical Research*, *97*(B3), 3285–3304. https://doi.org/10.1029/91JB02176

Uehara, K., & Saito, Y. (2019). Tidal amplitude decreases in response to estuarine shrinkage: Tokyo Bay during the Holocene. Estuarine. *Coastal Shelf Science*, *225*, 106225. https://doi.org/10.1016/j.ecss.2019.05.007

Uehara, K., Scourse, J. D., Horsburgh, K. J., Lambeck, K., & Purcell, A. P. (2006). Tidal evolution of the northwest European shelf seas from the Last Glacial Maximum to the present. *Journal of Geophysical Research*, *111*(C9), 1–15. https://doi.org/10.1029/2006JC003531

Vacchi, M., Engelhart, S. E., Nikitina, D., Ashe, E. L., Peltier, W. R., Roy, K., et al. (2018). Postglacial relative sea-level histories along the eastern Canadian coastline. *Quaternary Science Reviews*, *201*, 124–146. https://doi.org/10.1016/j.quascirev.2018.09.043

Vasskog, K., Svendsen, J.-I., Mangerud, J., Agasøster, H. K., Svean, A., & Lunnan, E. M. (2019). Evidence of early deglaciation (18 000 cal a bp) and a postglacial relative sea-level curve from southern Karmøy, south-west Norway. *Journal of Quaternary Science*, *34*(6), 410–423. https://doi.org/10.1002/jqs.3109

Velay-Vitow, J., & Peltier, W. R. (2020). Out of the ice age: Megatides of the Arctic Ocean and the Bølling-Ållerød, Younger Dryas transition. *Geophysical Research Letters*, *47*, 1–10. https://doi.org/10.1029/2020GL089870

Velay-Vitow, J., Peltier, W. R., & Stuhne, G. R. (2020). The tides of the glacial ocean and their possible connection to Heinrich event instabilities of the Laurentide ice sheet. *Journal of Geophysical Research: Oceans*, *125*, 1–23. https://doi.org/10.1029/2019JC015444

Wang, X., Verlaan, M., Apecechea, M. I., & Lin, H. X. (2021). Computation-efficient parameter estimation for a high-resolution global tide and surge model. *Journal of Geophysical Research: Oceans*, *126*(3), 1–24. https://doi.org/10.1029/2020JC016917

Ward, S. L., Neill, S. P., Scourse, J. D., Bradley, S. L., & Uehara, K. (2016). Sensitivity of palaeotidal models of the northwest European shelf seas to glacial isostatic adjustment since the Last Glacial Maximum. *Quaternary Science Reviews*, *151*, 198–211. https://doi.org/10.1016/j.quascirev.2016.08.034

Wessel, P., Luis, J. F., Uieda, L., Scharroo, R., Wobbe, F., Smith, W. H. F., & Tian, D. (2019). The generic mapping tools version 6. *Geochemistry, Geophysics, Geosystems*, *20*(11), 5556–5564. https://doi.org/10.1029/2019GC008515

Wilmes, S.-B, Schmittner, A., & Green, J. A. M. (2019). Glacial ice sheet extent effects on modeled tidal mixing and the global overturning circulation. *Paleoceanography and Paleoclimatology*, *34*(8), 1437–1454. https://doi.org/10.1029/2019PA003644

Wilmes, S.-B., & Green, J. A. (2014). The evolution of tides and tidal dissipation over the past 21,000 years. *Journal of Geophysical Research: Oceans*, *119*(7), 4083–4100. https://doi.org/10.1002/2013JC009605

Wunsch, C. (2003). Determining paleoceanographic circulations, with emphasis on the Last Glacial Maximum. *Quaternary Science Reviews*, *22*(2–4), 371–385. https://doi.org/10.1016/S0277-3791(02)00177-4

Zhang, X., Lohmann, G., Knorr, G., & Xu, X. (2013). Different ocean states and transient characteristics in Last Glacial Maximum simulations and implications for deglaciation. *Climate of the Past*, *9*(5), 2319–2333. https://doi.org/10.5194/cp-9-2319-2013